Cement and Concrete Research 159 (2022) 106871

Contents lists available at ScienceDirect

Cement and Concrete Research

journal homepage: www.elsevier.com/locate/cemconres

Solubility and characterization of synthesized 11 Å Al-tobermorite

B. Lothenbach [a,b,*,1], D. Jansen [c,1], Y. Yan [a], J. Schreiner [c]

[a] Empa, Concrete & Asphalt Laboratory, 8600 Dübendorf, Switzerland
[b] NTNU, Department of Structural Engineering, Trondheim, Norway
[c] Friedrich-Alexander-Universität Erlangen-Nürnberg, GeoZentrum Nordbayern, Mineralogy, Schlossgarten 5a, 91054 Erlangen, Germany

ARTICLE INFO

Keywords:
Al-tobermorite
Solubility
Thermodynamic data
XRD
NMR, FTIR Raman spectroscopy

ABSTRACT

The structure and solubility of hydrothermally prepared 11 Å Al-tobermorite with Al/(Al + Si) = 0.1 has been studied. NMR and FTIR data indicated the formation of a cross-linked, well crystalline 11 Å Al-tobermorite and preferential uptake of Al in the branching sites of the silicate chains. The incorporation of Al in branching sites of 11 Å tobermorite increased the basal spacing of the 11 Å Al-tobermorite by ~0.18 Å. Solubility experiments indicated little effect of temperature on the solubility of 11 Å Al-tobermorite and a weak stabilization of 11 Å Al-tobermorite with regard to 11 Å tobermorite. The experimental data confirmed the strong similarity in structure, Al-uptake, and solubility with poorly ordered C-A-S-H gel, although C-A-S-H gels showed a lower degree of ordering, the absence of cross-linking, an increased basal spacing, and a higher solubility.

1. Introduction

Reducing of the CO_2 emissions associated with cement production, which are around 800 kg per metric ton of manufactured cement, is currently one of the most important and urgent research topics within the cement community. A promising strategy to lower these CO_2 emissions is to reduce the clinker content by partially replacing Portland cement with supplementary cementitious materials (SCMs) such as blast furnace slags, fly ashes or calcined clays [1–4]. The use of such SCMs affects the composition, structure and properties of the main hydrate phase, calcium (alumino) silicate hydrate (C-(A-)S-H) gel, by increasing the SiO_2 and Al_2O_3 content in the hydrated cements. The solubility of C-S-H and its ability to bind aluminum are key parameters for predicting the stable phase composition of hydrating cements. The changes in thermodynamic properties and structure of C-A-S-H have received considerable attention due to their relevance for Portland cement (PC) and PC blended with SCMs [5–9].

The structure of the poorly ordered C-S-H gels is related to a defective tobermorite structure. Thus, much of the knowledge about C-S-H structure as well as modern thermodynamic models for describing C-A-S-H solubility are based on the knowledge about the tobermorite mineral group [10–12]. The main building blocks in C-A-S-H and in tobermorite are the so-called “dreierketten” (alumina)silicate chains, which are flanked on one side by the interlayer and on the other by calcium oxide sheets. The main differences between the hydrothermally synthesized 11 Å Al-tobermorite and poorly crystalline C-A-S-H gels prepared at room temperature are the degree of ordering, an increased basal spacing and the absence of cross-linked silica sites in the C-A-S-H samples. Hence, an improved understanding of crystalline 11 Å tobermorite minerals in terms of structure and solubility and the effect of Al substitution can significantly contribute to the scientific understanding of calcium (alumino) silicate hydrate gels.

Calcium silicate hydrate minerals belonging to the tobermorite group can be characterized by a basal spacing of approximately 11 Å and an orthorhombic sub-cell symmetry, which is the case for the 11 Å Al-tobermorite synthesized in this study [15]. Note, not all minerals in the tobermorite group have orthorhombic symmetry and a basal spacing of 11 Å [16]. For the synthesized tobermorite in this study, the word tobermorite is used in reference to 11 Å tobermorite. Aluminum can replace silicon in the bridging sites of the silicate chains [15]. In the case of partial substitution of silicon by aluminum the charge balance is restored through substitution of O^2 by OH^- in the silicon tetrahedron [13]. Hence, a general formula of tobermorite can be written as $Ca_{4+x}(Al_ySi_{6-y})O_{15+2x-y}(OH)_{2-2x+y}\cdot 5H_2O$ [15]. Consequently, the crystallochemical formula corresponds to $Ca_5[Si_6O_{17}]\cdot 5H_2O$ for a tobermorite without Al substitution and a Ca/Si ratio of 0.83, while a tobermorite with a Ca/Si ratio of 0.83 and Al/(Al + Si) = 0.1 as synthesized in this work, would be described as $Ca_5(Al_{0.6}Si_{5.4})$

* Corresponding author at: Empa, Concrete & Asphalt Laboratory, 8600 Dübendorf, Switzerland.
E-mail address: barbara.lothenbach@empa.ch (B. Lothenbach).
[1] Both authors contributed equally

https://doi.org/10.1016/j.cemconres.2022.106871
Received 24 December 2021; Received in revised form 20 May 2022; Accepted 7 June 2022
Available online 16 June 2022

$O_{16.4}(OH)_{0.6}$·5 H_2O or in the correct crystallochemical formula as $Ca_5[H_{0.6}Si_{5.4}Al_{0.6}O_{17}]$·$5H_2O$.

The structure of 11 Å tobermorite (double chain tobermorite, orthorhombic subcell), consists of infinite layers of CaO polyhedra, with tetrahedral silicate chains on both sides of such layers. The silicate chains are made of repeating units of two pairing silicates connected to the CaO main layer and a bridging silicate linked to the next pairing silicates forming long silica chains as illustrated in Fig. 1. The silicate chains are negatively charged, which is compensated by additional Ca^{2+} in the interlayer, where in addition water is present. Compositional variation caused by different calcium and water contents in the interlayer gives tobermorite group end-members of $Ca_4Si_6O_{15}(OH)_2$·$5H_2O$ and $Ca_5Si_6O_{17}$·$5H_2O$. The differences in the chemistry result in a different thermal behavior. According to Mitsuda and Taylor [17], tobermorites with a low Ca/Si ratio (e.g. 0.66 for $Ca_4Si_6O_{15}(OH)_2$·$5H_2O$) show an "anomalous" behavior, i.e. showing no decrease in basal spacing if heated, while increasing Ca content would lead to a so called "normal" behavior. It was additionally observed, that "anomalous" 11 Å tobermorite contained a significant Al component as well as alkalis [17].

The Ca rich endmember of 11 Å tobermorite is characterized by a Ca/Si molar ratio of 0.8333 and a cross-linking between adjacent silicate chains [13]. Based on the Loewenstein rule of Al-O-Al link avoidance [18], only one of two cross-linking sites can be occupied by Al, resulting in a maximum Al occupancy of $^1/_6$ of the tetrahedral sites of the silicate chain ($Al/Si_{max} = 0.2$, $Al/(Al + Si)_{max} = 0.17$). In contrast, for poorly ordered C-A-S-H gels, where cross-linked bridging sites are largely absent [7], a higher maximum Al-uptake of up to $^1/_3$ of the tetrahedral sites of the silicate chain ($Al/Si_{max} = 0.5$, $Al/(Al + Si)_{max} = 0.33$) could theoretically be possible in an infinite silicate chain [19]. The presence of aluminum accelerates the formation of tobermorite under hydrothermal conditions [20,21] and leads to a stabilization of Al-tobermorite relative to tobermorite [22]. The substitution of silicon by aluminum leads to an increase in the basal spacing (lattice parameter c) and decreased crystal domain size in the a-direction, which can be detected by applying an anisotropic crystallite size model combined with Rietveld refinement, as observed in numerous XRD and NMR studies [20,23–30]. In addition, at high aluminum dosage ($Al/(Al + Si) \geq 0.15$) the presence of crystalline katoite ($Ca_3Al_2(OH)_{12}$) is observed [31], where Al is present in octahedral coordination.

Only a few thermodynamic data sets [5,32,33] and solubility measurements for tobermorite [33,34] have been reported in the literature. The solubility products for tobermorite reported in the literature vary considerably from 10^{-45} to 10^{-52} (Table 1) or $10^{-7.5\ to-8.7}$ if scaled to contain 1 mol of silicon, while for amorphous C-A-S-H gels with Ca/Si between 0.8 and 0.85, solubility products of $\approx 10^{-8.0}$ are reported in the absence and presence of Al [35–38]. No measured solubility data are available for Al-containing tobermorite.

The present work is focused on hydrothermally synthesized 11 Å Al-tobermorite as a crystalline proxy for calcium (alumina) silicate hydrate (C-A-S-H). The structure of 11 Å Al-tobermorite and its solubility are investigated between 3 and 60 °C based on experimental data and thermodynamic modelling.

2. Materials and methods

2.1. Synthesis procedure

The raw materials used for the synthesis of Al-tobermorite included quartz flour (> 99.5 % SiO_2, verified by XRF analysis, from Rotilab), calcium hydroxide (synthesized from $CaCO_3$ > 99.95 %, from Alfa Aesar), aluminum hydroxide (> 99.9 %, from Alfa Aesar) and deionized water. Thermogravimetric analysis (TGA) confirmed the absence of additional water in calcium hydroxide and aluminum hydroxide and the presence of <0.5 wt% of CO_2 in calcium hydroxide. The weight proportions of the solid raw materials were calculated and conformed to the molar ratios $Ca/(Si + Al) = 0.83$ and $Al/(Al + Si) = 0.1$, thus correspond to a 11 Å Al-tobermorite: $Ca_5[H_{0.6}Si_{5.4}Al_{0.6}O_{17}]$·$5H_2O$.

The solid raw materials were first weighed and later homogenized in a laboratory mill. The water-to-solid ratio was fixed at 3 and the slurry was prepared by manual stirring for 1 min at 23 °C. A PTFE-lined stainless steel autoclave was used for the hydrothermal treatment. After 20 h at 180 °C and 1.1 MPa autogenous steam pressure, the autoclave was cooled to ambient temperature and the sample was removed for drying. After drying at 60 °C for 12 h, the sample was

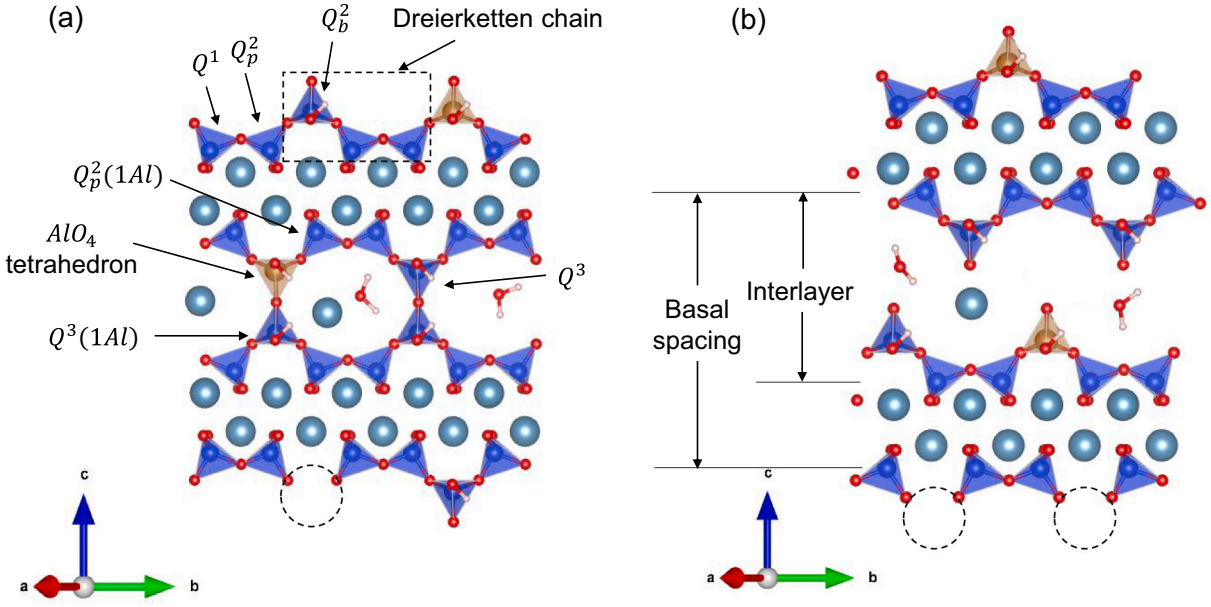

Fig. 1. The arrangement of (a) cross-linked (based on the tobermorite structure from Merlino et al. [13]) and (b) non-cross-linked tobermorite-like structures. Blue, gold, turquoise, red and white spheres represent Si, Al, Ca, O and H, respectively and dashed circles vacancies in bridging sites. Q^n: n indicates the numbers of Si tetrahedral neighbors, b: bridging position, p: pairing position. Visualization realized with VESTA [14]. (For interpretation of the references to colour in this figure legend, the reader is referred to the web version of this article.)

Table 1
Thermodynamic properties of tobermorite, SiO_2, Al_2O_3 and structural water at 298 K and 1 bar pressure.

	log K_{s0}[a]	$\Delta_f G°$	$\Delta_f H°$	S°	C_p	Vol	Reference
		kJ/mol	kJ/mol	J/mol/K	J/mol/K	cm^3/mol	
11 Å-tobermorite: $Ca_5Si_6O_{17}·5.5H_2O$	−49.46	−9889.25	−10,680.92	692.55	764.91	286.2	[5]
	−49.25	−9880.31	−10,695.56	611.49	698.52		[32]
	−44.8 to −52.4						[33]
SiO_2 (quartz)		−856.287	−910.70	41.46	44.60	22.69	[39,40]
Al_2O_3(corundum)		−1582.26	−1675.70	50.92	79.03	25.59	[39,40]
structural H_2O				40.2	40.0	13.7	[41]

[a] $K_{S0,tobermorite} = \{Ca^{2+}\}^5·\{HSiO_3^-\}^6·\{OH^-\}^4·\{H_2O\}^{0.5}$; {} denotes activities. Scaled to 6 mol of silicon.

ground using an agate mortar.

2.2. Solid phase characterization techniques

2.2.1. XRD

The XRD data of the synthesized sample was measured with a D8 DaVinci diffractometer (Bruker AXS; CuK$\alpha_{1,2}$; 0.5° divergence slits; 2.5° soller slits; elimination of CuK$_\beta$ by Lynx Eye Detector). The measurements were recorded from 5° to 75°2Θ with a step size of 0.02°2Θ and 0.5 s/step. After 120 days, the sample was measured again with equal parameters following storage at 60 °C in aqueous solution. The XRD data was evaluated using the Rietveld analysis [42] combined with an external standard method [43,44]. Rietveld refinement was done using Topas *V*.5 from Bruker AXS applying the fundamental parameters approach [45]. Crystallographic structures of tobermorite (orthorhombic sub-cell), quartz and calcite were used for Rietveld refinement respectively [46–48].

The domain morphology of Al-tobermorite was verified based on anisotropic peak broadening [25,49]. The synthesized tobermorite was heat treated at 300 °C for 2 h and measured again applying the same parameters in order to investigate whether the tobermorite synthesized is a “normal” or an “anomalous” tobermorite [17].

2.2.2. TGA

Thermogravimetric analysis (TGA) was performed on about 50 mg of the powder using a NETSCH STA 449 F1 Jupiter under nitrogen atmosphere with a heating rate of 5 °C/min between room temperature and 1000 °C. Both the curve for relative weight change and the differential mass loss were plotted and used for qualitative assignment of the mass loss during drying.

2.2.3. ^{27}Al and ^{29}Si NMR

^{29}Si MAS NMR single-pulse experiments were recorded using a Bruker Advance III NMR spectrometer with a 7 mm CP/MAS probe and applying 79.5 MHz. Additionally, 4500 Hz was used for the sample rotation rate and a minimum of 3072 scans were recorded. 30° ^{29}Si pulse of 2.5 us was used and 20 s relaxation delays. The RF field strength was 33.3 kHz during SPINAL64 proton decoupling. The chemical shifts recorded were referenced using tetramethylsilane (TMS, d29Si = 0.00 ppm). The deconvolution of the recorded data was done by least squares fitting applying Lorentzian and Gaussian functions (50/50), considering the structural restraints imposed by the tobermorite structure, i.e. the presence of two Q_p^2 pairing sites for each bridging Q_b^2 site: $Q_p^{2*} = 2Q_b^2$ (where Q_p^{2*} equals to Q_p^2 pairing corrected for cross-linked sites: $Q_p^{2*} = Q_p^2 - 2(Q^3 + Q^3(1Al))$ and the presence of at least two $Q_p^2(1Al)$ pairing sites for each cross-linked $Q^3(1Al)$ site: $Q_p^2(1Al) \geq 2\ Q^3(1Al)$ as detailed in Myers et al. [7,10]. The discussion is based on Q^n classification of the Si tetrahedron, where n varies from 1 to 4 giving the number of further connected Si or Al tetrahedrons.

^{27}Al MAS NMR measurements were carried out using a 2.5 mm CP/MAS probe. The single-pulse experiments for ^{27}Al MAS NMR were recorded with 104.26 MHz. The parameters used in the present study are 20 kHz spinning speed, 4000 scans, π/12 pulses of 1 ms without 1H decoupling, and 1 s relaxation delays. In order to reference the chemical shifts of the ^{27}Al MAS NMR spectra, 1.0 mol/l $AlCl_3·6H_2O$ solution was used at 0 ppm. The discussion is based on q^n classification of the Al tetrahedron, where n varies from 1 to 4 giving the number of connected Si tetrahedrons.

2.2.4. FTIR

ATR-FTIR (attenuated total reflectance Fourier-transform infrared) spectra were measured using a Bruker Tensor 27 FTIR spectrometer with a diamond ATR crystal. 32 scans were recorded and averaged focusing on the transmittance between 340 cm^{-1} and 4000 cm^{-1} with a resolution of 4 cm^{-1}. Approximately 5 mg of powder were used. The software package of Bruker (OPUS 8.2 SP2) was used for baseline correction. The recorded spectra were normalized to the intensity of the peak around 960 cm^{-1}.

2.2.5. Raman

Raman spectra were acquired using a WITec Alpha 300 R confocal Raman microscope in backscattering geometry. A diode-pumped green laser with a wavelength of 532 nm laser was used in combination with a 50 × objective lens. The Rayleigh scattered light was blocked by an edge filter. The backscattered light was coupled to a 300 mm lens-based spectrometer with a grating of 600 g/mm equipped with a cooled deep-depletion CCD. Back- illuminated CCD chip with 1024 × 127 pixel format, pixel size 26 × 26 μm. The laser output power was set to 20 mW, the integration time was 10 s and each spectrum was recorded 10 times. The tobermorite samples showed strong efflorescence. Spectral analysis was conducted using Spectragryph and the spectra have been normalized to the most intensive band at ≈ 670 cm^{-1} [50].

2.3. Solubility experiments

The synthesized and ground sample was stored in aqueous solutions in four batches at 3, 23, 40, and 60 °C for 120 days in order to reach the respective equilibria. All of the vessels were sealed with Parafilm. The samples were shaken once per week. After 30, 60, 90, and 120 days of storage, a small amount of solution (approximately 2 ml) was taken to determine pH and aqueous concentrations and filtered through a 200 nm filter in order to remove any solid particles.

The pH values were determined from a small aliquot of the undiluted solutions equilibrated to 20 °C due to practical reasons (pH meter Mettler Toledo SevenCompact, equipped with pH electrode N6000bc from SI Analytics; calibrated with pH 7.0 (Roth, A518.2), 9.0 (Roth, A519.1), and 12.0 (Roth, T189.2) standard solutions). ICP-MS analyses were performed on acidified (HNO_3 Suprapur) and diluted solutions, in order to avoid any precipitation between sampling and measurement. The total concentrations of Ca, Si, and Al were measured quantitatively using quadrupole inductively coupled plasma mass spectrometry, applying the standard addition approach for Si (Q-ICP-MS).

The solid fraction of the sample stored at 60 °C for 120 days was oven dried at 40 °C and investigated by XRD analysis in order to verify the phase composition and the basal spacing of 11 Å Al-tobermorite.

2.4. Thermodynamic modelling

Thermodynamic modelling was carried out using the Gibbs free energy minimization program GEMS [51,52]. GEMS is a broad-purpose geochemical modelling code which computes equilibrium phase assemblage and speciation in a complex chemical system from its total bulk composition. Thermodynamic data for aqueous and solid species were taken from the GEMS-PSI thermodynamic database [53,54]. The measured total concentrations of Ca, Si and Al in the solution were used to calculate ion activity and the solubility of Al-containing tobermorite (downscaled to contain 0.9 mol of silicon and 0.1 mol of aluminum) $Ca_{0.83}H_{0.1}Si_{0.9}Al_{0.1}O_{2.83}$ $(H_2O)_{0.83}$ according to Eq. (1):

$$K_{S0,Al-tobermorite} = \{Ca^{2+}\}^{0.833}\cdot\{HSiO_3^-\}^{0.9}\cdot\{AlO_2^-\}^{0.1}\cdot\{OH^-\}^{0.666}\cdot\{H_2O^0\}^{0.1} \quad (1)$$

The activity of Ca^{+2}, $HSiO_3^-$, AlO_2^-, OH^-, and H_2O^0, {i} was calculated with the help of GEMS using the measured total concentrations of Al, Ca and Si and considering the formation of different aqueous complexes. The activity of a species, {i}, equals $\{i\} = \gamma_i \cdot m_i$, where γ_i is the activity coefficient and m_i the concentration of the species or complex in mol/kg H_2O. The dimensionless activity coefficients (−), γ_i, were computed with the extended Debye-Hückel equation according to Eq. (2):

$$log\gamma_i = \frac{-A_y z_i^2 \sqrt{I}}{1 + B_y a_i \sqrt{I}} + b_y I \quad (2)$$

A common ion-size parameter a_i of 3.72 Å for NaCl solutions and common third parameter b_y (~0.64 for NaCl electrolyte at 25 °C) as integrated in GEMS are used. z_i denotes the charge of species i, I the effective molar ionic strength, and A_y and B_y are P,T-dependent coefficients. This activity correction is applicable up to approx. 1 mol/kg_w ionic strength [55].

The measured total concentrations in the solution were also used to calculate the saturation index (SI) of gibbsite and quartz: $SI = \log_{10}(IAP/K_{S0})$. IAP is the ion activity product calculated from the measured total solution concentrations and K_{S0} is the equilibrium solubility product from the GEMS-PSI thermodynamic database [53,54].

The thermodynamic data for (Al)-tobermorite at temperatures other than 25 °C was calculated using the temperature dependence of the apparent Gibbs free energy of formation from the element, $\Delta_a G°$, according to Eq. (3):

$$\Delta_a G^o_T = \Delta_f G^o_{T_0} - S^o_{T_0}(T - T_0) - \int_{T_0}^{T}\int_{T_0}^{T} \frac{C^o_p}{T} dTdT$$
$$= \Delta_f G^o_{T_0} - S^o_{T_0}(T - T_0) - a_0\left(Tln\frac{T}{T_0} - T + T_0\right) - 0.5a_1(T - T_0)^2$$
$$-a_2\frac{(T - T_0)^2}{2T\cdot T_0^2} - 2a_3\frac{\left(\sqrt{T} - \sqrt{T}_0\right)^2}{\sqrt{T_0}} \quad (3)$$

where a_0, a_1, a_2, and a_3 are the empirical coefficients of the heat capacity equation $C°_p = a_0 + a_1T + a_2T^{-2} + a_3T^{-0.5}$, T (K) the experimental temperature, while 298.15 K corresponds to the reference temperature T_0. The apparent Gibbs free energy of formation, $\Delta_a G°_T$, corresponds at 298.15 K to the Gibbs free energy of formation, $\Delta_f G°_{T0}$. The above calculation is integrated in the GEMS-PSI code. A more detailed description of the derivation of the temperature dependence of the Gibbs energy is given in the online documentation of GEMS [56], or in [57].

No measured entropy or heat capacity data are available for Al-containing tobermorite, thus these data were estimated from the entropy and heat capacity data of 11 Å-tobermorite, corundum(C), structural water (H) and quartz(Q), as summarized in Table 1 following the procedure outlined in Helgeson et al. [41]. The entropy of Al-tobermorite, $Ca_{0.83}H_{0.1}Si_{0.9}Al_{0.1}O_{2.83}\cdot 0.83H_2O$, was estimated form 11 Å tobermorite, $Ca_{0.83}SiO_{2.83}\cdot 0.83H_2O$, according to Eq. (62) in [41]: $S_{Al\text{-}Tob} = (S_{Tob} - 0.1S_Q + 0.05S_C + 0.05S_H)\cdot(V°_{Tob} - 0.1V_Q + 0.05V_C + 0.05V_H + V°_{Al\text{-}Tob})/2/(V°_{Tob} - 0.1V_Q + 0.05V_C + 0.05V_H)$, taking into account the effect of molar volume. The C_p was calculated from the heat capacity of the different solids $C_{p,Al\text{-}Tob} = (C_{p,Tob} - 0.1C_{p,Q} + 0.05C_{p,C} + 0.05C_{p,H})$, assuming $\Delta C_{p,r} = 0$ following Eq. (78) in [41].

3. Results

3.1. Solid-phase analysis

3.1.1. XRD

The results of powder XRD analysis are given in Fig. 2 and show that Al-tobermorite was successfully synthesized along with minor amounts of calcite and quartz. The quantification of the sample using the external standard yields 81 wt% of crystalline sample and 19 wt% amorphous phase. The amorphous content is most likely due to the presence of some non-crystalline C-A-S-H. The refinement of the synthesized 11 Å Al-tobermorite shows good agreement with the orthorhombic sub-cell symmetry reported for the tobermorite group.

The synthesized 11 Å Al-tobermorite was heated up to 300 °C and measured again in order to show whether the tobermorite can be assigned to a "normal" tobermorite or "anomalous" tobermorite. According to Merlino et al. [15], a tobermorite that shows a decrease in basal spacing from 11.3 Å to 9.3 Å can be assigned to the structure of a "normal" tobermorite, while a "anomalous" tobermorite shows no decrease in basal spacing after heating. As shown in Fig. 3, the tobermorite synthesized in this study shows a decrease in basal spacing and consequently can be described as a "normal" tobermorite. These findings are also in line with the literature, where it is reported that replacing silicon with aluminum leads to a "normal" tobermorite, while higher amounts of alkalis would lead to an "anomalous" one [21,29,58]. The synthesized tobermorite shows "normal" behavior, which points towards the Ca–rich endmember $Ca_5[H_{0.6}Si_{5.4}Al_{0.6}O_{17}]\cdot 5H_2O$ [17].

For the synthesized 11 Å Al-tobermorite, a basal spacing of 11.3 Å was determined for the (002) reflection, as well as a unit cell volume of 474 Å for the $Ca_5[H_{0.6}Si_{5.4}Al_{0.6}O_{17}]\cdot 5H_2O$ composition. The refinement was done based on the structure suggested by Hamid et al. [46]. The increase of the basal presence and lattice parameter c (22.8 Å) complies with values reported in previous studies on Al-tobermorite [59]. In accordance with the results in previous studies [44,49], the anisotropic peak broadening indicated that the presence of Al in tobermorite resulted in a reduced crystallinity in a direction (perpendicular to the silicate chains).

Fig. 4 summarizes reported basal spacing for synthesized tobermorites with and without Al and illustrates that the 11 Å Al-tobermorite synthesized in this study shows a basal spacing comparable to the spacings reported in the literature for Al-tobermorite. The presence of Al in tobermorite clearly increases the basal spacing due the substitution of Si in the bridging sites by Al, as Al—O bonds are about 8–10 % longer than Si—O bonds [31,60]. Thus, the increase of the basal spacing determined by means of X-ray diffraction and Rietveld analysis is a reliable indicator for the incorporation of Al in the structure of the synthesized Al-tobermorite.

Rietveld analysis was also used to assess possible changes during the equilibration in aqueous solutions to determine the solubility of 11 Å Al-tobermorite (Fig. 5). No new phases appeared and no significant dissolution was observed to occur during the solubility experiments. Slightly more calcite was present in the stored sample, most likely due to carbonation during the second drying step. The basal spacing did not change during the experiments, as seen in the constant position of (002) reflection (Fig. 2), indicating that the original 11 Å Al-tobermorite species remained structurally intact during the solubility experiments.

3.1.2. Water content

TGA results are shown in Fig. 6, where the differential mass loss as

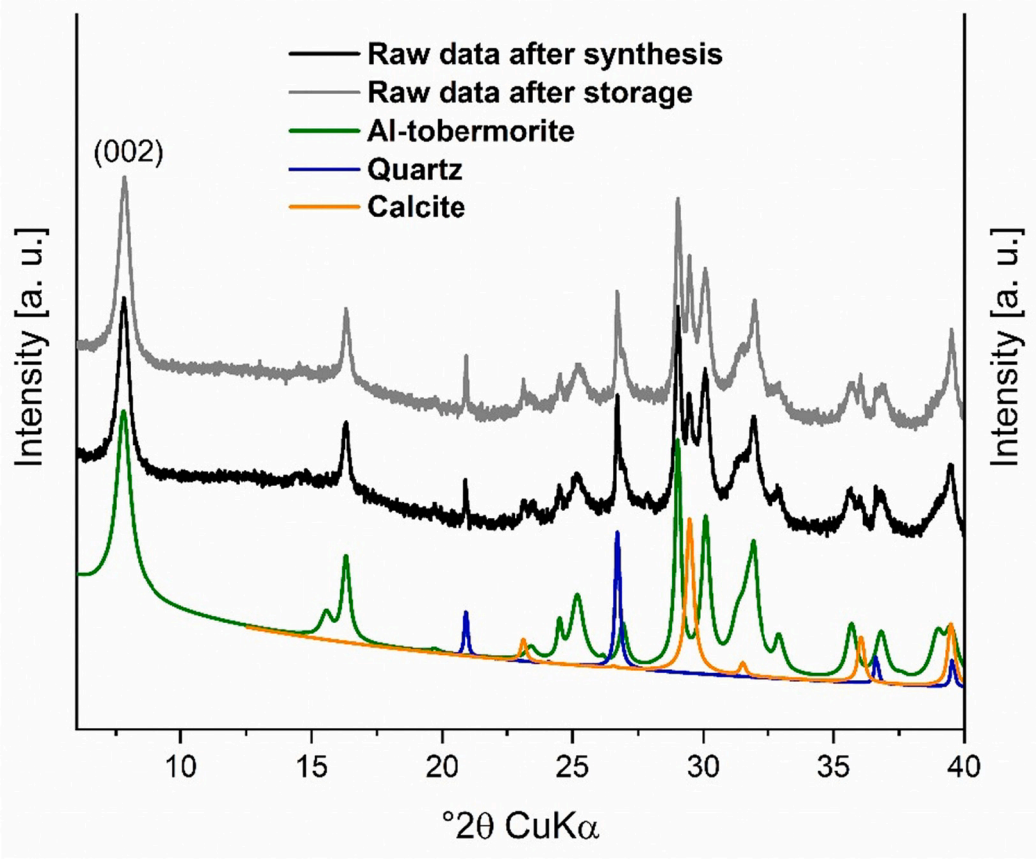

Fig. 2. XRD patterns of the synthesis product before and after storage for 120 days at 60 °C with calculated fits of crystalline phases therein.

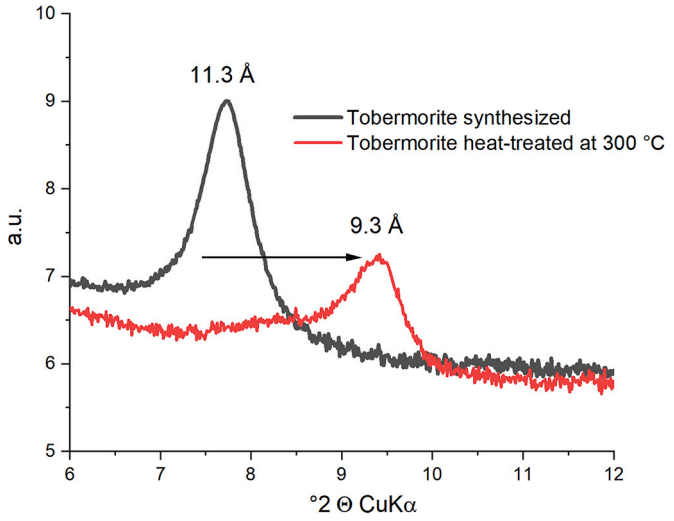

Fig. 3. Shift of (002) reflex of 11 Å Al-tobermorite after heating to 300 °C, indicating that the synthesized 11 Å Al-tobermorite is a "normal" tobermorite.

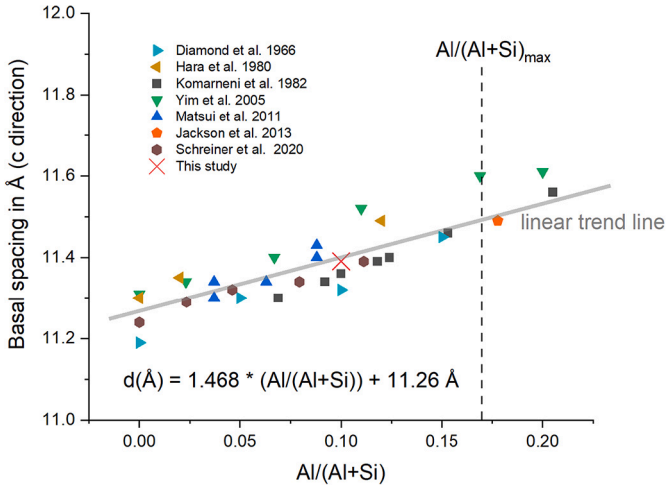

Fig. 4. Basal spacing (d) in c-direction vs Al/(Al + Si) as reported in literature and from synthesized 11 Å Al-tobermorite (assuming complete Al uptake in tobermorite; all reported Ca/Si ratios between 0.8 and 0.9). Theoretical maximum Al occupancy $^{1}/_{6}$ in silicate chain: $Al/(Al + Si)_{max} = 0.17$. Data from [22,24,26,29,61–63].

well as the relative sample mass are plotted against temperature. The weight loss between 80 °C and 150 °C can be assigned to the weight loss due to loosely bound and interlayer water of the Al-tobermorite, comparable to the temperature region where the water loss of tobermorite [27,64] and of C-A-S-H [7] is observed. An additional weight loss is present between 400 °C and 600 °C. A comparable weight loss was described for tobermorite by Yu et al. [65], who assigned it to an amorphous phase. This weight loss was also reported by Myers et al. [7] for C-A-S-H samples prepared at 80 °C, but not for samples prepared at 5, 20, or 50 °C. They reported this weight loss only for samples where cross-linking between the silicate chains was observed by ^{29}Si NMR, while [37] observed this signal also for C-A-S-H samples at 20 °C, where no cross-linking was reported. Together this could indicate that cross-linked C-A-S-H and 11-Å tobermorite loses a part of the interlayer water at a higher temperature than non-cross-linked C-A-S-H samples or the formation of an un-identified amorphous phase. The weight loss

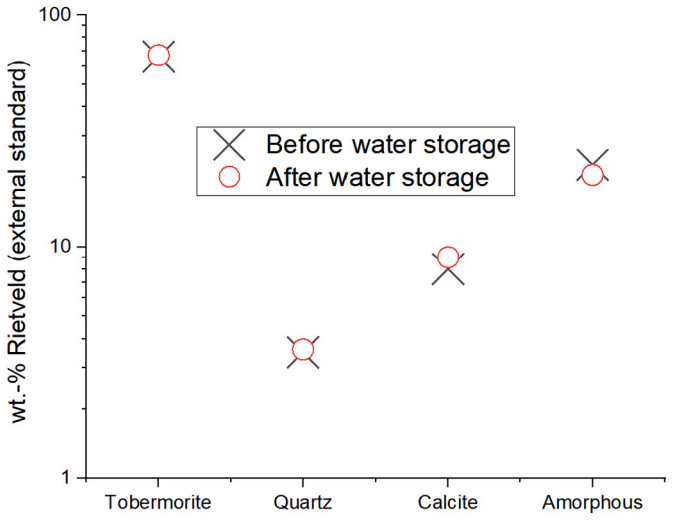

Fig. 5. Rietveld results of the 11 Å Al-tobermorite synthesized before and after equilibration in water at 60 °C for 120 days.

between 600 and 650 °C is due to the presence of some calcite in the sample (as also observed by XRD, Fig. 2), while the signal at 800 °C is associated with loss of the OH group due to destabilization of tobermorite to wollastonite at this temperature [7,27].

The total measured weight loss is 15 wt% of the sample, which can be separated into around 12 wt% of water loss from the dehydration of the Al-tobermorite (up to 600 °C), 3 wt% of CO_2 loss due to the decarbonation of calcite present in the sample and a little weight loss of OH groups due to wollastonite formation. The observed weight loss of around 12 wt% is in line with the expected weight loss of 12.32 wt% expected for 11 Å tobermorite, $Ca_5[Si_6O_{17}]\cdot 5H_2O$ [13], indicating a comparable water content in 11 Å Al-tobermorite: $Ca_5[H_{0.6}Si_{5.4}Al_{0.6}O_{17}]\cdot 5H_2O$ (with a theoretical weight loss of 12.33 wt%). The measured weight loss of Al-tobermorite is lower than the weight loss of ≈ 20 wt% observed for poorly ordered C-A-S-H gels with a comparable composition [35,37].

3.1.3. Si and Al-NMR

The ^{29}Si MAS NMR spectra of Al-tobermorite shows several bands, which can be assigned to an Al-substituted cross-linked tobermorite structure (Fig. 1, Fig. 7). Bands at −80.2 ppm, −82.7 ppm, −84.2 ppm and − 85.8 ppm are visible, which were assigned to Q^1, Q^2_p(1Al), Q^2_b(bridging), and Q^2_{pa} (pairing) silica species [66,67], respectively, indicating the presence of Al in the silicate chain. Another Q^2_{pb} band can be detected at −88.5 ppm [68]. In addition, cross-linked Q^3(1Al) and Q^3 (see Fig. 7 and Table 2) sites can be detected at −91.9 ppm and -96.6 ppm as previously reported in [7,69], indicating that both Si and Al are present in the branching sites (Q^3) in Al-tobermorite, supporting previous observations [10,18,70] that aluminum is not present in pairing Q^2_p and/or Q^1 sites. The presence of roughly 2.2 times as much Q^2_p(1Al) as Q^3(1Al) sites indicates that most of the Al is present in the cross-linked branching sites and little (20 % or less) in non-cross-linked bridging Q^2_b sites. This is in agreement with mesoscale Monte Carlo simulations and first-principle calculations, which showed that Al is more likely to substitute for Si at cross-linking sites than at bridging sites [19,71].

Based on the structural arrangement of the silicate chains in so-called "dreierketten" (see Fig. 1), the mean chain length (MCL_c, the average number of aluminosilicate tetrahedral in a cross-linked, as indicated by the subscript $_c$, tobermorite-like chain) as well as the molar Al/Si_c ratios were calculated using Eqs. (4) and (5) for the cross-linked C-A-S-H structures as detailed in Myers et al. [7,10] and Richardson [72]:

$$MCL_c = \frac{4\left[Q^1 + Q^2 + Q^2(Al) + Q^3 + 2Q^3(Al)\right]}{Q^1} \quad (4)$$

$$Al \Big/ Si_c = \frac{Q^3(Al)}{Q^1 + Q^2 + Q^2(Al) + Q^3 + Q^3(Al)} \quad (5)$$

A mean chain length of 23 was calculated for the synthesized 11 Å Al-tobermorite, comparable to a MCL_c of 23 to 28 calculated from the Si NMR data for hydrothermally prepared Al-tobermorite [27,64,73], but somewhat shorter than the MCL_c of ≈70 calculated for an Na-containing Al-tobermorite using the data reported by [69]. Note that the Al-tobermorite has more Q^1 sites (≈20 %), Q^2_b (≈5 %) sites and a lower MCL than11 Å tobermorite without Al, where MCL > 100 have been

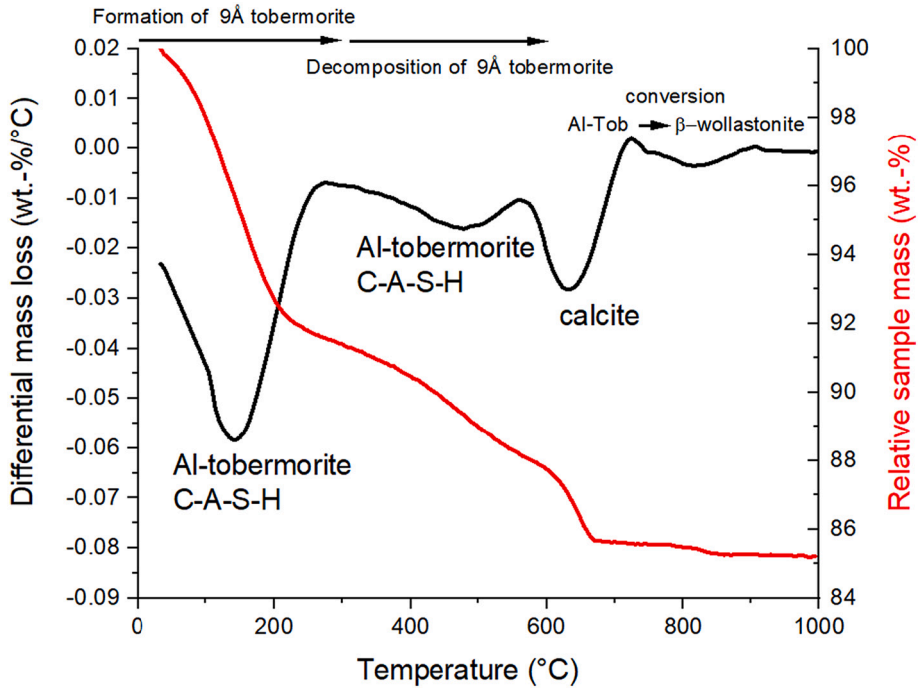

Fig. 6. Differential mass loss and relative sample mass of the synthesized 11 Å Al-tobermorite measured by TGA.

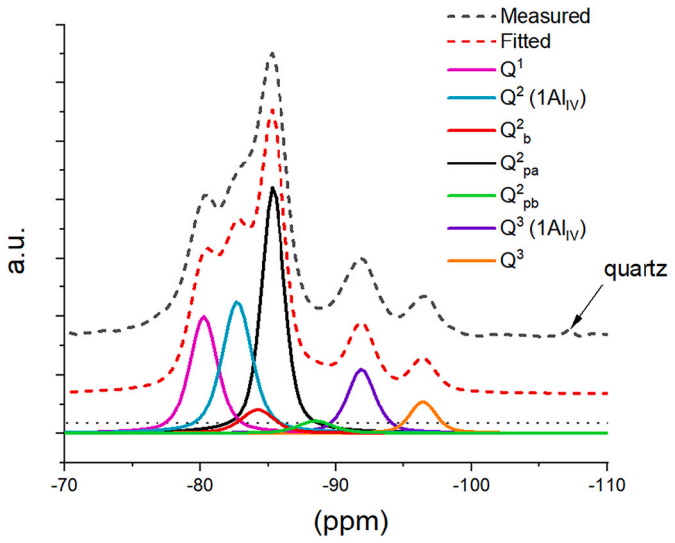

Fig. 7. ^{29}Si MAS NMR results and fitted spectra for the Al-tobermorite synthesized in the present study.

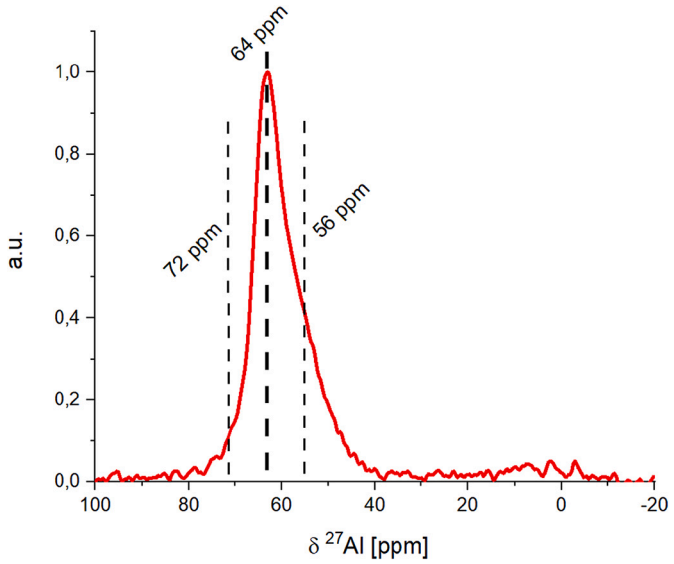

Fig. 8. ^{27}Al MAS NMR of the 11 Å Al-tobermorite synthesized in the present study. The dashed lines indicate the main band at 64 (Al_{iso} = 66) and a minor band at 56 (Al_{iso} = 56) ppm (both assigned to branching Al: q^3(3Si)) with a different chemical environment and a shoulder at ≈72 assigned to a minor amount of bridging Al: q^2(2Si).

Table 2
Results from ^{29}Si MAS NMR of 11 Å Al-tobermorite.

Band position (ppm)	Silicate species	Fraction[a] (%)
−80.2	Q^1	19.6
−82.7	Q^2(1Al)	23.7
−84.2	Q^2_b	4.6
−85.8	Q^2_{pa}	34.2
−88.5	Q^2_{pb}	2.6
−91.9	Q^3(1Al)	10.6
−96.6	Q^3	4.6
Mean chain length[b]		22.6
Al/Si[c]		0.106

[a] $Q^{2*}_p = 2Q^2_b$ ($Q^{2*}_p = Q^2_p - 2(Q^3 + Q^3(1Al))$ and $Q^2_p(1Al) \geq 2\ Q^3(1Al)$, see [7].
[b] Calculated using Eq. (4).
[c] Calculated using Eq. (5).

reported [73], indicating that Al in tobermorite lowers the degree of polymerization in agreement with the observations of [27,59,73]. This decrease in polymerization in the presence of aluminum seems to indicate that a (minor) part of the bridging Al and Si sites in Al-tobermorite are not cross-linked.

In addition, the MCL of C-S-H and C-A-S-H samples synthesized at room temperature is with 20 to 27 comparable [35,74]. The main difference between the hydrothermally synthesized 11 Å Al-tobermorite and poorly crystalline C-A-S-H gels prepared at room temperature is the absence of cross-linked silica sites in the C-A-S-H samples, which, however, does not significantly lower the calculated MCL. For C-A-S-H samples prepared at elevated temperature (50 °C in the presence of alkali, at 80 °C without alkalis) in addition to C-A-S-H, the formation of some 11 Å tobermorite and the presence of cross-linked Q^3(1Al) and Q^3 sites has been observed as well as an increase in the MCL [7,75].

The calculated Al/Si value of the sample is 0.106, which is in agreement with the weighed initial amounts. The high Al/Si also confirms a complete uptake of Al in the tobermorite structure, in agreement with preparations of Al-tobermorite reported in literature, where Al/Si up to ≈0.2 has been observed [27,69].

The ^{27}Al MAS NMR spectrum for the 11 Å Al-tobermorite sample as given in Fig. 8 shows a main signal at ≈62–66 ppm indicating the presence of tetrahedrally coordinated Al(IV). The position of this band agrees with previous studies on Al-tobermorite, where signals at ≈ 64 ppm have been reported for Al-tobermorite [27,59,62,64,76,77]. In many cases, a second band at ≈ 56 ppm with varying intensities has also been reported. The sites had previously been assigned to Al in bridging (q^2(2Si)) at ≈ 64 ppm and branching (or cross-linking) q^3(3Si) sites at ≈56 ppm [64,69,78]. Based on our ^{29}Si NMR data (Table 2), which generally showed that most Al is present in branching sites, the assignment of the band at ≈64 ppm to Al in bridging (q^2(2Si)) sites appears questionable. At 64 ppm, the signal is at a frequency that is around 5 to 10 ppm lower than the signals at 76 and 68 ppm assigned to Al connected to two silica in the bridging sites, q^2(2Si), in C-A-S-H [68,78]. With increasing numbers of bridging oxygen connected to Al, an increase in the shielding and a lower shift is expected [79] and thus the band at 64 is tentatively assigned to a branching (or cross-linking) q^3(3Si) site. The band at ≈ 56 ppm reported in some preparations of Al-tobermorite was not clearly observed (<10 %) in the 11 Å Al-tobermorite prepared in the present study (Fig. 8). This minor band at 56 ppm might be also assigned to a q^3(3Si) either in the vicinity of Ca (or Na), which can lower the isometric shift by several ppm, [80] or to a q^3(3Si) further away from the next Al, as an increase of SiO_2 content in glasses results in a low-frequency shift of the Al resonance [81–84]. Only a minor amount of Al in bridging position (signal at 68–76 ppm [68,78]) is observed, in agreement with the Si NMR data. No significant bands can be seen for $^{(V)}$Al coordination at 25 ppm or for $^{(VI)}$Al between 20 ppm and 0 ppm, in agreement with previous studies on Al-tobermorite [27,62,69,76,77].

In C-A-S-H samples with Ca/Si = 0.8 prepared at ambient temperatures, generally tetrahedral $^{(IV)}$Al coordination sites at ≈76 ppm and ≈68 ppm have been observed, which both have been assigned to Al in the unbranched bridging sites, q^2(2Si), of the C-A-S-H silicate chains [35,68,71,78,85,86].

3.1.4. FTIR and Raman

The FTIR and Raman spectra of 11 Å Al-tobermorite, of a C-S-H sample with $Ca/Si_{C\text{-}S\text{-}H}$ = 0.88 and of a C-A-S-H sample with target Al/Si = 0.1 and Ca/(Si + Al) = 0.73 are compared in Fig. 9. The second derivative spectra of FTIR are added to read overlapping bands and make the band position easier to identify. The vibrational spectra can be divided into three types: bands due to CO_3^{2-} vibration, bands due to water molecules and O–H group vibrations, and bands due to silicate (aluminate) tetrahedral vibrations, those including from Al-tobermorite and quartz.

Asymmetric stretching of C–O appears on the FTIR as a broad band

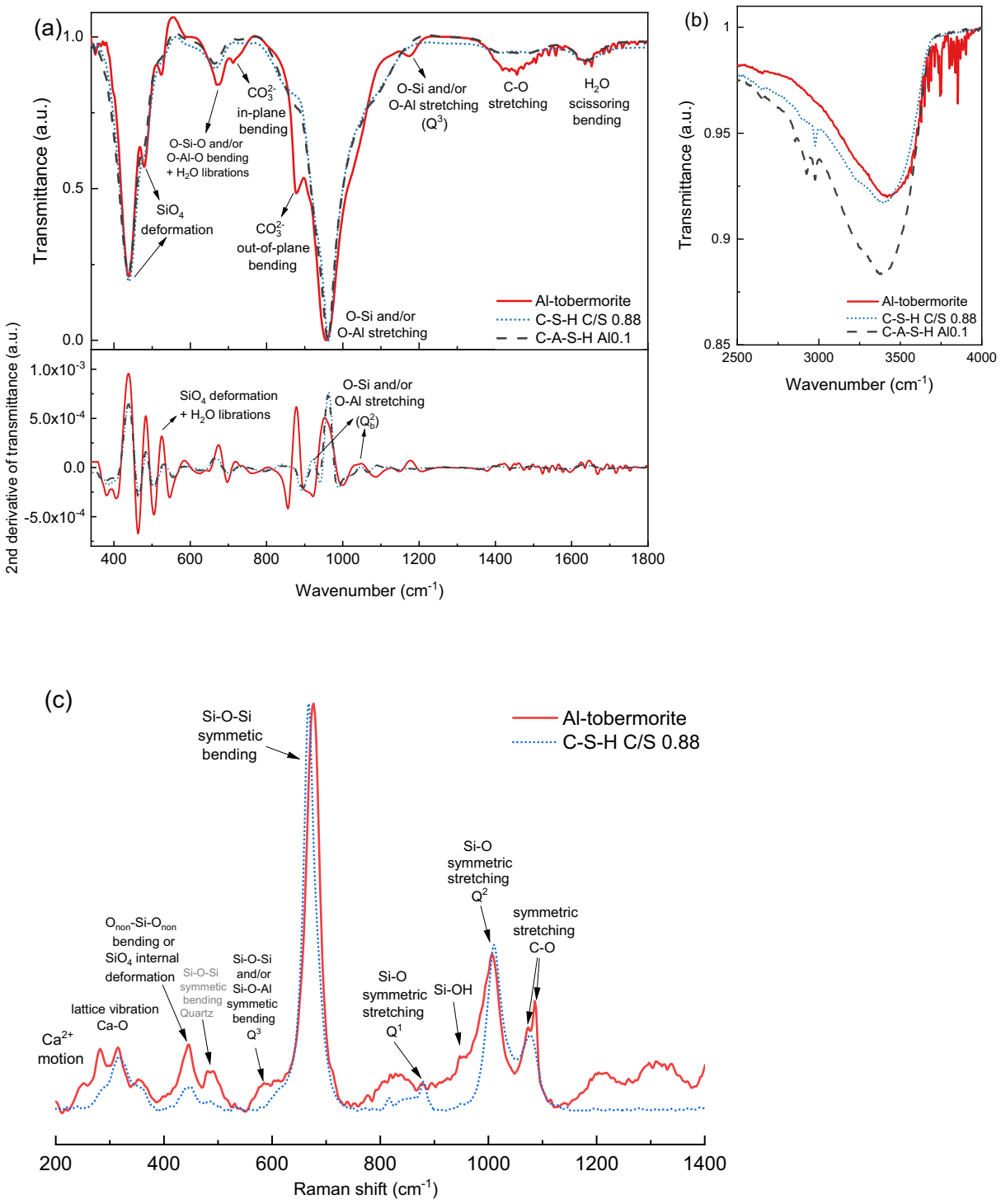

Fig. 9. (a) FTIR finger-print region, (b) FTIR -OH region, and (c) Raman of Al-tobermorite (this paper), C-S-H ($Ca/Si_{C\text{-}S\text{-}H}$ = 0.88, without Al, equilibrated for 3 months, from [74]) and C-A-S-H (target Al/Si = 0.1, Ca/(Si + Al) = 0.73) equilibrated for 2 years, from [37]).

for C-A-S-H and several small peaks at 1350–1570 cm^{-1}. The bands at 715 and 877 cm^{-1} in Al-tobermorite are due to the in-plane and out-of-plane bending of CO_3^{2-}, due to the presence of some calcite in the sample as observed by XRD and TGA. The presence of calcite is also visible in the band at 1086 cm^{-1}.

The intensive, broad FTIR band located at 2500–3700 cm^{-1} indicates the asymmetric stretching modes of O–H from water [74,87,88]. A narrow band at 2981 cm^{-1} from the C-A-S-H can be assigned to the O–H stretching from ethanol, used to wash the C-A-S-H samples [37]. The scissoring bending signal of water appears at 1632 cm^{-1}. The band at 670 cm^{-1} can be partially attributed to water librations [88].

The FTIR bands in the region of 800–1200 cm^{-1} are due to stretching vibration of O–Si–O and/or O-Al–O, while SiO_4 and/or AlO_4 deformation, bending vibrations of the O–Si–O and/or O–Al–O groups in the dreierketten chains and from water liberations [74,87] are visible from 400 cm^{-1} to 800 cm^{-1}; the band at 670 cm^{-1} is related to O–Si–O and/or O–Al–O bending and water librations. In general, Al-tobermorite shows better resolved and defined O–Si and/or O–Al vibration bands than

those of C-A-S-H, in agreement with the crystalline structure of the Al-tobermorite and poorly crystallite feature of C-A-S-H structure.

The most intense FTIR peak in Al-tobermorite and the C-A-S-H appears as a complex group of bands in the range of 900–1100 cm^{-1}, attributed to asymmetrical stretching vibrations of Si–O. The second derivative of transmittance indicates the presence of two signals, a main band at ~920 cm^{-1} and a shoulder at 1050 cm^{-1}, which are assigned to the Si–O stretching of Q^2 silicate (aluminate) tetrahedra [74,88,89]. Also the Raman band at 950–1010 cm^{-1} has been assigned to symmetrical stretching Q^2 [90–93], and the shoulder at 950 cm^{-1}, observed for Al-tobermorite, to Si–OH stretching vibrations [73]. The Q^3 bands in Raman are expected at slightly higher wavenumbers (1050–1100 cm^{-1}) [91,94,95], which overlaps with the carbonate signal. For C-S-H an additional SS Q^1 band at ~870–900 cm^{-1} is present. Additional Raman bands are present at 800–900 cm^{-1} and 1200–1400 cm^{-1}, which have been reported in previous studies in C-A-S-H and Al-tobermorite [26,93], but not assigned. Part of the signal at around 800 cm^{-1} and 1080–1170 cm^{-1} could be due to the presence of quartz [96,97].

The intense bands from 400 to 550 cm^{-1} in FTIR and Raman are assigned to deformations of Si tetrahedra [69,74,89] or to O–Si–O bending [70]. The band located at 438 cm^{-1} in FTIR and at 445 cm^{-1} in Raman is assigned to deformations of Si tetrahedral and the FTIR bands at 484 and 524 cm^{-1} to the bending vibration of O–Si–O and/or O–Al–O and Si–O–Si and/or Si–O–Al [98]. The Raman bands between 200 cm^{-1} to 400 cm^{-1}, are due to Ca^{2+} motions and Ca–O lattice vibrations [91,92]. The peak at 480 cm^{-1} is assigned to O–Si–O bending from quartz [96].

The band at ≈1170 cm^{-1} in FTIR is characteristic of Al-tobermorite and assigned to Si–O and/or Al–O stretching of Q^3 silicate (aluminate) tetrahedra [59,89,98]. Also the Raman spectra in Fig. 9c highlights some characteristics of Al-tobermorite. The main Si–O–Si bending peak in Raman at 676 cm^{-1} and the main Si–O stretching peak in FTIR at 957 cm^{-1} of Al-tobermorite is broader than the one of C-A-S-H, due to the presence of an additional Al(Si)- OH band, at slightly lower wavenumbers than the Si– OH band [73]. In addition, a broad shoulder at ~560–620 cm^{-1} in Al-tobermorite indicates the presence of Q^3 sites, symmetrical bending of Si-O-Si and/or Si-O-Al [26,73,91].

The presence of aluminum in the tetrahedral sites of Al-tobermorite has been reported to result in a lowering of the wavenumber of the stretching Q^3 vibrations in FTIR at 1200 cm^{-1} as well as of the stretching O—Si and/or O—Al at 970 cm^{-1} [27,64,98]. The band position of Q^3 and of the most intensive O—Si and/or O—Al stretching at ≈ 970 cm^{-1} were plotted versus Al/Si in tobermorite and C-A-S-H in Fig. 10. A clear linear decrease of the wavenumber with increasing Al content is found for Q^3 O–Si and/or O–Al stretching band. Similarly, a lowering of the wavenumber for general O–Si(Al) stretching modes is observed with additional Al, but associated with more scattering as the position of the stretching band at 970 cm^{-1} is influenced by the incorporated Al in two different ways. The replacement of silica by alumina in tobermorite lowers the $\langle \upsilon_{Si-O} \rangle$ [87], while a lower Ca/(Si + Al) and thus a higher polymerization degree shifts the signal to a higher wavenumber [89]. This opposing trends explain why in the case of C-A-S-H, where the addition of Al decreases the Ca/(Si + Al), no clear shift has been observed, while in the case of tobermorite, where Si has been replaced by Al at a constant Ca/(Si + Al), a decrease of $\langle \upsilon_{O-Si(Al)} \rangle$ is observed (see e.g. dataset of Liao et al. [27] in Fig. 10 (b)), although some scatter is observed between the different literature sources [27,64,89,98]. The linear correlation of the Q^3 signal suggests that FTIR can be used similarly as XRD to assess the Al/Si in tobermorite or cross-linked C-A-S-H based on the O–Si(Al) stretching Q^3 band position.

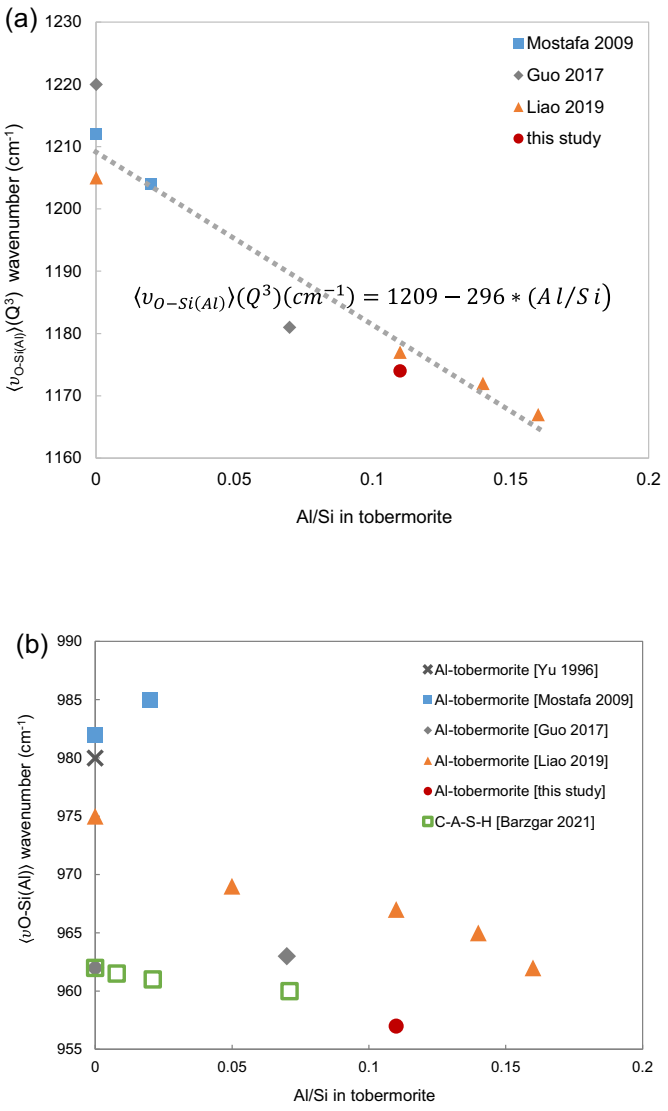

Fig. 10. Correlation between (a) wavenumber of Q^3 stretching vibrations (O–Si (Al)) in FTIR and Al/Si ratio in tobermorite (Al/Si = (1209-ν_{Q3} [cm^{-1}])·0.00352) and (b) wavenumber of O-Si(Al) stretching vibrations in FTIR and Al/Si ratio in tobermorite and C-A-S-H gels. Solid symbols: tobermorite from [27,64,89,98] and this study; empty symbols: C-A-S-H from [37]. Note that Yu et al. [89], Mostafa et al. [98] and Liao et al. [27] used transmission FTIR, while Guo et al. [64], Barzgar et al. [37] and this study used ATR FTIR.

3.2. Solubility

3.2.1. Aqueous phase composition

At all temperatures studied, a moderate increase in the concentrations of Al, Ca, and Si over time was observed between 30 and 60 days as shown in Fig. 11 and Table 3, while no significant differences were observed between 60 and 120 days, indicating a slow dissolution of the synthesized 11 Å Al-tobermorite such that equilibrium was reached only after 2 months and longer. Similar to our observations, Dickson et al. [33] reported a slow equilibration for pre-synthesized tobermorite. The solutions were moderately undersaturated with respect to gibbsite and quartz (Table 3).

In most cases, somewhat higher calcium concentrations than silicon concentrations were measured, which could indicate a slightly increased availability of calcium in the tobermorite. At 60 °C, however, an increase in silicon and a decrease in calcium concentration is observed at longer equilibration times as well as a slight decrease in Al concentration after >60 days. This could indicate some dissolution of quartz at 60 °C, as those solution became slightly less undersaturated with respect to quartz after 90 and 120 days (Table 3) or a possible re-arrangement in the Al-tobermorite structure over time. This change, however, is only visible at the elevated temperature of 60 °C and not associated with any

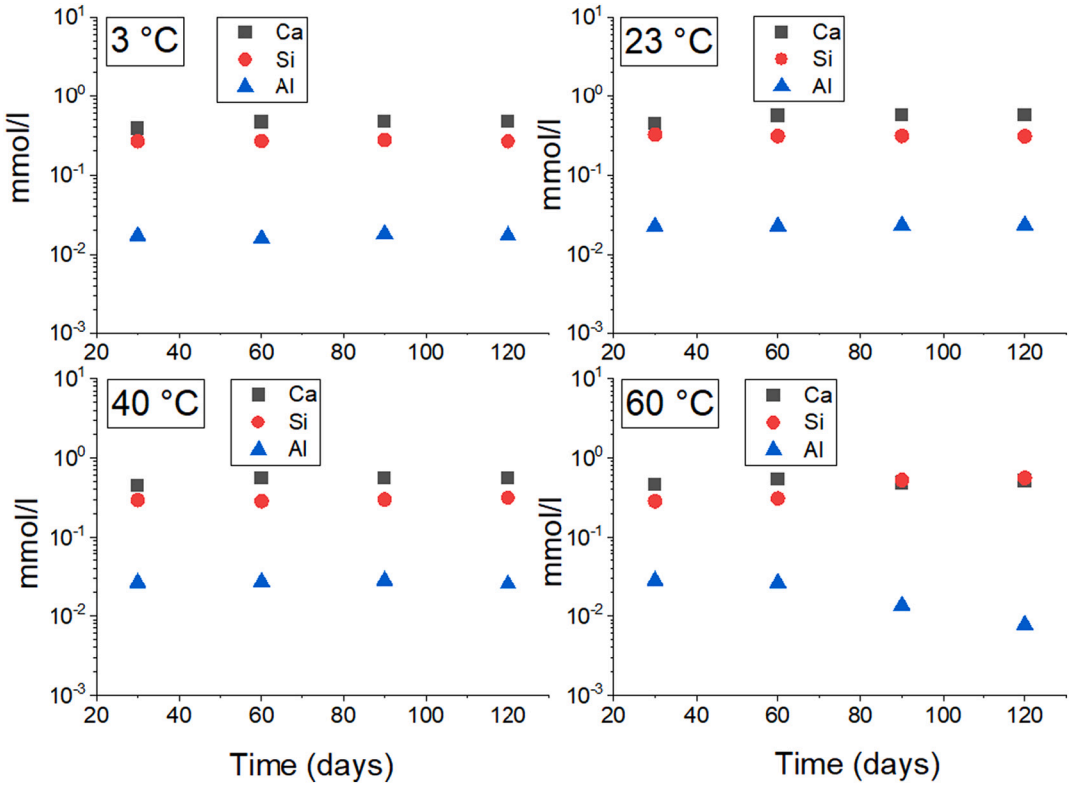

Fig. 11. Measured total concentrations of Ca, Si and Al at 3, 23, 40, and 60 °C as a function of time.

Table 3
Measured total concentrations of Ca, Si and Al at 3, 23, 40, and 60 °C GEMS calculated and measured pH values, and saturation indices (SI) of quartz and gibbsite as a function of time.

Equilibration time (days)	Ca (mmol/l)	Si (mmol/l)	Al (mmol/l)	pH[a]	pH[b]	pH[c]	SI gibbsite[d]	SI quartz[d]
3 °C								
30	0.38	0.26	0.017	11.5	11.3	10.7	0.0	−0.8
60	0.46	0.27	0.016	11.6	11.3	10.7	−0.2	−1.0
90	0.47	0.28	0.018	11.6	11.3	10.7	−0.1	−0.9
120	0.47	0.26	0.017	11.6	11.3	10.7	−0.2	−1.0
23 °C								
30	0.44	0.32	0.023	10.8	10.7	10.9	−0.2	−0.7
60	0.56	0.31	0.023	10.9	10.7	10.8	−0.4	−0.9
90	0.56	0.31	0.023	10.9	10.5	10.7	−0.4	−0.9
120	0.56	0.31	0.023	10.9	10.6	10.8	−0.4	−0.9
40 °C								
30	0.45	0.30	0.026	10.3	10.3	10.9	−0.4	−0.8
60	0.56	0.29	0.027	10.4	10.1	10.7	−0.6	−0.9
90	0.56	0.30	0.028	10.4	10.1	10.8	−0.5	−0.9
120	0.56	0.32	0.025	10.4	10.1	10.8	−0.6	−0.9
60 °C								
30	0.46	0.28	0.028	9.8	9.8	10.9	−0.7	−0.8
60	0.53	0.31	0.026	9.9	9.5	10.7	−0.8	−0.8
90	0.48	0.53	0.013	9.8	9.5	10.6	−0.9	−0.5
120	0.51	0.56	0.008	9.8	9.4	10.6	−1.2	−0.5

[a] pH calculated based on measured total concentrations.
[b] pH corrected from 20 °C to 3 °C (+0.65), to 23 °C (−0.10), to 40 °C (−0.63) and to 60 °C (−1.14); effect of temperature on pH calculated by GEMS.
[c] pH measured at 20 °C.
[d] Calculated saturation indices (SI) with respect to quartz and gibbsite.

obvious decrease of the amount of quartz as shown in Fig. 2 and Fig. 5.

The total Al/Si used in the experiments corresponded to 0.11, while the Al/Si in the aqueous phase varied between 0.05 and 0.09, indicating a slight preference of tobermorite to incorporate Al over Si. This is in agreement with experimental observations in C-A-S-H gels, where much lower Al than Si concentrations were observed [7,9,35–37,99] as well as with molecular calculations, which indicate a moderate stabilization of Al compared to Si in the bridging sites of C-A-S-H gels [71,100].

The temperature had relatively little effect on the measured concentrations, in agreement with the observations reported for tobermorite [33,34] as well as for C-A-S-H [7,38,75].

3.2.2. Solubility product of the synthesized 11 Å Al-tobermorite

Based on the measured elemental concentrations of Ca, Si and Al, the solubility product of 11 Å Al-tobermorite ($K_{S0,Al\text{-}tobermorite} = \{Ca^{2+}\}^{0.833} \cdot \{HSiO_3^-\}^{0.9} \cdot \{AlO_2^-\}^{0.1} \cdot \{OH^-\}^{0.666} \cdot \{H_2O^0\}^{0.13}$) was calculated and the data are summarized in Fig. 12. At all temperatures studied, a moderate increase in the solubility product of Al-tobermorite by ≈ 0.2 log units was observed between 30 and 60 days, while no significant differences were observed between 60 and 120 days, again underlining that the synthesized Al-tobermorite was close to equilibrium within the first 60 days. Note although the concentrations of Ca and Si are reversed at 60 °C between 60 and 90 days, there is no significant effect on the calculated solubility product.

The solubility products calculated at 23, 40, and 60 °C showed comparable values of $\approx 10^{-8.55\pm0.1}$, while at 3 °C a lower solubility product of $10^{-8.76}$ was obtained. A comparable behavior has been observed for C-A-S-H, where no significant difference was observed between 20 and 80 °C, while a lower value was observed for C-A-S-H with Ca/Si = 1.0 at 5 °C [7]. In contrast to those observations, Glasser et al. [38] reported for C-S-H a moderate decrease in solubility with temperature. However, this could be related to the observed formation of crystalline tobermorite at 85 °C after 4.5 months [38].

In Fig. 13, the mean of the solubility products calculated for 11 Å Al-tobermorite after 60, 90, and 120 days are compared to the solubility products of 11 Å tobermorite based on the few available experimental data in literature [33,34,38] as well as compared to the solubility product calculated for C-S-H and C-A-S-H with Ca/Si = 0.8 or 0.85 [35–38]. Most of the solubility products for 11 Å tobermorite (diamonds) are comparable or only slightly higher than the solubility product of Al-tobermorite (circles), with the exception of the tobermorite solubility product at 25 °C from Dickson et al. [33,101] (note that the solubility products calculated based on the values reported at 25 °C by [33,101] vary largely between $10^{-8.8}$ to $10^{-7.2}$, indicating a significant scatter in that set of experiments). In contrast, the solubility product of $10^{-8.5}$ measured by Hong [34] for tobermorite at 25 °C is only slightly higher than the value obtained here for Al-tobermorite. At higher temperatures, very similar solubility products were also measured for tobermorite and Al-tobermorite [33,38], indicating an only weak

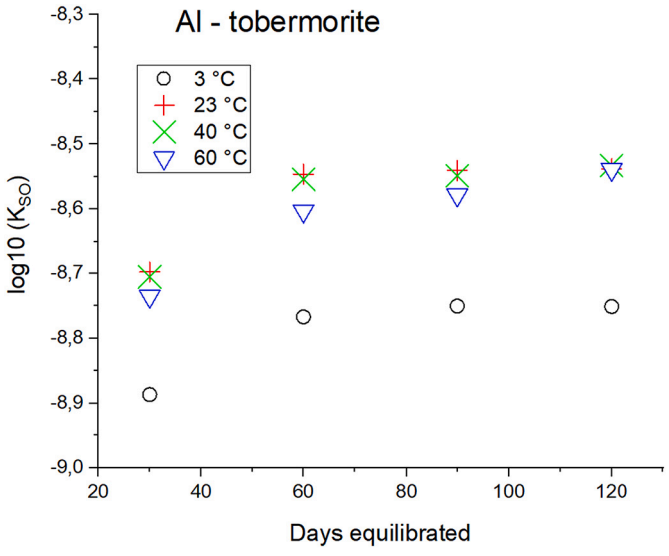

Fig. 12. Calculated solubility product of 11 Å Al-tobermorite ($K_{S0,Al\text{-}tobermorite} = \{Ca^{2+}\}^{0.833} \cdot \{HSiO_3^-\}^{0.9} \cdot \{AlO_2^-\}^{0.1} \cdot \{OH^-\}^{0.666} \cdot \{H_2O^0\}^{0.13}$) as a function of equilibration time.

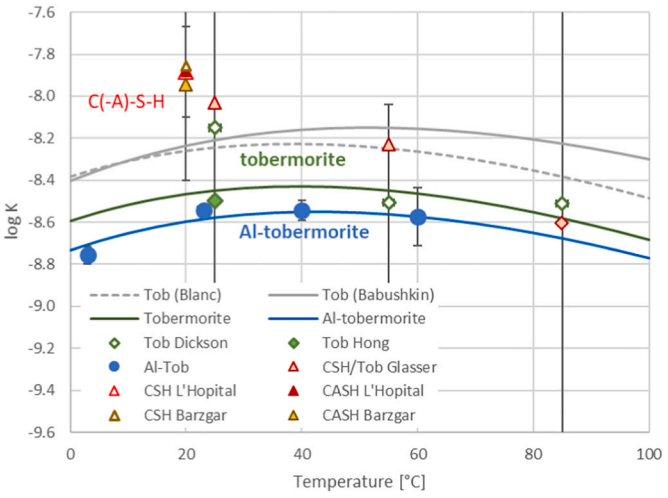

Fig. 13. Calculated solubility product of 11 Å Al-tobermorite ($K_{S0,Al\text{-}tobermorite} = \{Ca^{2+}\}^{0.833} \cdot \{HSiO_3^-\}^{0.9} \cdot \{AlO_2^-\}^{0.1} \cdot \{OH^-\}^{0.666} \cdot \{H_2O^0\}^{0.1}$, circles) measured between 56 and 120 days compared to the solubility of 11 Å tobermorite (diamonds, $K_{S0,-tobermorite} = \{Ca^{2+}\}^{0.833} \cdot \{HSiO_3^-\} \cdot \{OH^-\}^{0.666}$; measurements reported in [33,34]), C-A-S-H (triangles, $K_{S0,CASH} = \{Ca^{2+}\}^{0.833} \cdot \{HSiO_3^-\}^{1-x} \cdot \{AlO_2^-\}^{x} \cdot \{OH^-\}^{0.666} \cdot \{H_2O^0\}^{x}$; measurements at Ca/Si = 0.8 and 0.85 of [35–38]) and calculated (lines) based on the thermodynamic data collected in Table 1 and Table 4.

preference for Al uptake over Si uptake in the bridging/branching sites of tobermorite. Thermodynamic data for tobermorite have also been reported by Blanc et al. [5] and Babushkin et al. [32] as summarized in Table 1; those data sets seem to overestimate the measured tobermorite solubility products by $10^{0.2}$ to $10^{0.3}$ units (Fig. 13, dotted and short-dashed lines).

At 20 to 25 °C, the solubility products of precipitated C-A-S-H gels (triangles) are approximately 4 times ($10^{0.6}$) higher than the solubility product of (Al-)tobermorite, as expected and in agreement with other studies [5]. Also in the case of C-S-H, an uptake of Al in its structure has only a very weak stabilizing effect on the solubility product of C-A-S-H gels (Fig. 13, [37,75]).

Based on the measured data, the solubility products of 11 Å tobermorite at 25 °C ($K_{S0,tobermorite} = \{Ca^{2+}\}^{0.833} \cdot \{HSiO_3^-\} \cdot \{OH^-\}^{0.666}$: $10^{-8.45\pm0.2}$) and 11 Å Al-tobermorite ($K_{S0,Al\text{-}tobermorite} = \{Ca^{2+}\}^{0.833} \cdot \{HSiO_3^-\}^{0.9} \cdot \{AlO_2^-\}^{0.1} \cdot \{OH^-\}^{0.666} \cdot \{H_2O^0\}^{0.1}$: $10^{-8.58\pm0.1}$) were derived as summarized in Table 4. The effect of temperature was obtained based on Eq. (3) using entropy and heat capacity data derived from tobermorite [5].

4. Conclusions

In this paper the structure and solubility of hydrothermally prepared 11 Å Al-tobermorite has been studied. XRD, NMR and FTIR data indicated the formation of a cross-linked, well crystalline 11 Å Al-tobermorite. Si NMR data indicated that all Al present (Al/Si = 0.11) was found in the silicate chain of tobermorite structure mainly within branching sites connected to two pairing silica sites, $Q^2(1Al)$, as well to a branching silica, $Q^3(1Al)$, in an adjacent silicate chain. The presence of aluminum in 11 Å tobermorite lowered somewhat the degree of polymerization compared to Al-free 11 Å tobermorite.

The uptake of aluminum in 11 Å tobermorite can be quantified based on the reduction of wavenumber of Q^3 Si(Al) vibrations in the FTIR spectra as well as on the increase of the basal spacing in XRD. The incorporation of Al (Al/Al + Si = 0.1) in 11 Å tobermorite increased the basal spacing by ~0.15 Å.

Dissolution experiments indicated that (near-)equilibrium was reached within 60 days at all temperatures. At 60 °C, however, the

Table 4
Thermodynamic properties of tobermorite and Al-tobermorite at 298 K and 1 bar pressure.

log K_{s0}	$\Delta_f G°$	$\Delta_f H°$	$S°$	C_p	Vol	Reference
	kJ/mol	kJ/mol	J/mol/K	J/mol/K	cm^3/mol	
11 Å tobermorite: $Ca_{0.83}SiO_{2.83}{\cdot}0.83H_2O$						
-8.45 ± 0.2[a]	−1628.34	−1755.35	112.5[b]	124.1[b]	46.89[c]	This study
Al-tobermorite: $Ca_{0.83}H_{0.1}Si_{0.9}Al_{0.1}O_{2.83}{\cdot}0.83H_2O$						
-8.58 ± 0.1[a]	−1634.08	−1762.85	114.1[d]	125.6[d]	47.57[e]	This study
11 Å tobermorite: $Ca_5Si_6O_{17}{\cdot}5H_2O$						
-50.7 ± 1.2	−9770.02	−10,532.09	674.9[b]	744.9[b]	281.35[c]	This study
Al-tobermorite: $Ca_5H_{0.6}Si_{5.4}Al_{0.6}O_{17}{\cdot}5H_2O \Leftrightarrow \{Ca^{2+}\}^5 \cdot \{HSiO_3^-\}^{5.4} \cdot \{AlO_2^-\}^{0.6} \cdot \{OH^-\}^4{\cdot}\{H_2O^0\}^{0.6}$						
-51.5 ± 0.6	−9804.62	−10,577.21	684.5[d]	753.9[d]	285.45[e]	This study

[a] $K_{S0,tobermorite} = \{Ca^{2+}\}^{0.833}{\cdot}\{HSiO_3^-\}{\cdot}\{OH^-\}^{0.666}$ and $K_{S0,tobermorite} = \{Ca^{2+}\}^5{\cdot}\{HSiO_3^-\}^6{\cdot}\{OH^-\}^4$; $K_{S0,Al\text{-}tobermorite} = \{Ca^{2+}\}^{0.833} \cdot \{HSiO_3^-\}^{0.9} \cdot \{AlO_2^-\}^{0.1} \cdot \{OH^-\}^{0.666} \cdot \{H_2O^0\}^{0.1}$ and $K_{S0,Al\text{-}tobermorite} = \{Ca^{2+}\}^5 \cdot \{HSiO_3^-\}^{5.4} \cdot \{AlO_2^-\}^{0.6} \cdot \{OH^-\}^4{\cdot}\{H_2O^0\}^{0.6}$.
[b] S and C_p adapted from water content of $Ca_5Si_6Al_{0.6}O_{17}{\cdot}5.5H_2O$ from Blanc et al. [5] to "normal" tobermorite: $Ca_5Si_6Al_{0.6}O_{17}{\cdot}5H_2O$ using structural water.
[c] Molar volume calculated from the volume of 467 $Å^3$ for $Ca_5Si_6O_{17}{\cdot}5H_2O$ [24].
[d] S and C_p calculated from 11-tobermorite [5], corundum, structural water and quartz, using additive methods described by Helgeson et al. [41].
[e] Molar volume calculated from the volume of 474 $Å^3$ obtained for $Ca_5H_{0.6}Si_{5.4}Al_{0.6}O_{17}{\cdot}5H_2O$.

decrease in Al-concentration and increase in Si concentrations indicated a possible dissolution of quartz or further structural rearrangement.

The solubility of 11 Å Al-tobermorite showed little change between 23 and 60 °C, while it was slightly less soluble at 3 °C. The comparison with solubility data reported for tobermorite indicated a small stabilization of 11 Å Al-tobermorite compared to 11 Å tobermorite with silica only. Both 11 Å Al-tobermorite and 11 Å tobermorite are more stable than poorly ordered C-A-S-H gel.

Comparison of 11 Å Al-tobermorite with data for poorly ordered C-A-S-H gels with a comparable composition underlined the strong similarity in structure, Al-uptake and solubility behavior between Al-tobermorite and C-A-S-H gels. The main difference between 11 Å Al-tobermorite and C-A-S-H gels is that the latter has a lower degree of ordering, no cross-linking between adjacent silicate chains, an increased basal spacing, as well as a somewhat higher solubility.

CRediT authorship contribution statement

B. Lothenbach: Conceptualization, Methodology, Investigation, Formal analysis, Writing – original draft, Visualization. **D. Jansen:** Conceptualization, Methodology, Investigation, Formal analysis, Writing – original draft, Visualization. **Y. Yan:** Methodology, Investigation, Formal analysis, Writing – original draft, Visualization. **J. Schreiner:** Methodology, Investigation, Formal analysis, Writing – original draft.

Declaration of competing interest

The authors declare that they have no known competing financial interests or personal relationships that could have appeared to influence the work reported in this paper.

Acknowledgement

The financial support of Y. Yan by the Swiss National Science Foundation (SNSF, grant no. 200021_169014) is gratefully acknowledged. Daniel Rentsch (Empa) is acknowledged for the measurement of the NMR data and Ellina Bernard for help with the interpretation of Al NMR data. The NMR hardware was partially supported by the Swiss National Science Foundation (SNSF, grant no. 206021_150638/1).

References

[1] M. Thomas, L. Barcelo, B. Blair, K. Cail, A. Delagrave, K. Kazanis, Lowering the carbon footprint of concrete by reducing clinker content of cement, Transp. Res. Rec. (2012) 99–104, https://doi.org/10.3141/2290-13.
[2] E. Gartner, Industrially interesting approaches to "low-CO2" cements, Cem. Concr. Res. 34 (2004) 1489–1498, https://doi.org/10.1016/j.cemconres.2004.01.021.
[3] P.J.M. Monteiro, S.A. Miller, A. Horvath, Towards sustainable concrete, Nat. Mater. 16 (2017) 698–699, https://doi.org/10.1038/nmat4930.
[4] K.L. Scrivener, V.M. John, E.M. Gartner, Eco-efficient cements: potential economically viable solutions for a low-CO2 cement-based materials industry, Cem. Concr. Res. 114 (2018) 2–26, https://doi.org/10.1016/j.cemconres.2018.03.015.
[5] P. Blanc, X. Bourbon, A. Lassin, E.C. Gaucher, Chemical model for cement-based materials: temperature dependence of thermodynamic functions for nanocrystalline and crystalline C-S–H phases, Cem. Concr. Res. 40 (2010) 851–866, https://doi.org/10.1016/j.cemconres.2009.12.004.
[6] B. Lothenbach, A. Nonat, Calcium silicate hydrates: solid and liquid phase composition, Cem. Concr. Res. 78 (2015) 57–70, https://doi.org/10.1016/j.cemconres.2015.03.019.
[7] R.J. Myers, E. L'Hôpital, J.L. Provis, B. Lothenbach, Effect of temperature and aluminium on calcium (alumino)silicate hydrate chemistry under equilibrium conditions, Cem. Concr. Res. 68 (2015) 83–93, https://doi.org/10.1016/j.cemconres.2014.10.015.
[8] J.R. Houston, R.S. Maxwell, S.A. Carroll, Transformation of meta-stable calcium silicate hydrates to tobermorite: reaction kinetics and molecular structure from XRD and NMR spectroscopy, Geochem. Trans. 10 (2009) 1, https://doi.org/10.1186/1467-4866-10-1.
[9] C. Roosz, P. Vieillard, P. Blanc, S. Gaboreau, H. Gailhanou, D. Braithwaite, V. Montouillout, R. Denoyel, P. Henocq, B. Madé, Thermodynamic properties of C-S-H, C-A-S-H and M-S-H phases: results from direct measurements and predictive modelling, Appl. Geochem. 92 (2018) 140–156, https://doi.org/10.1016/j.apgeochem.2018.03.004.
[10] R.J. Myers, S.A. Bernal, R. San Nicolas, J.L. Provis, Generalized structural description of calcium-sodium aluminosilicate hydrate gels: the cross-linked substituted tobermorite model, Langmuir 29 (2013) 5294–5306, https://doi.org/10.1021/la4000473.
[11] D.A. Kulik, G.D. Miron, B. Lothenbach, A structurally-consistent CASH+ sublattice solid solution model for fully hydrated C-S-H phases: thermodynamic basis, methods, and ca-si-H2O core sub-model, Cem. Concr. Res. 151 (2022), 106585, https://doi.org/10.1016/j.cemconres.2021.106585.
[12] G.D. Miron, D.A. Kulik, Y. Yan, J. Tits, B. Lothenbach, Extensions of CASH+ thermodynamic solid solution model for the uptake of alkali metals and alkaline earth metals in C-S-H, Cem. Concr. Res. 152 (2022), 106667, https://doi.org/10.1016/j.cemconres.2021.106667.
[13] S. Merlino, E. Bonaccorsi, T. Armbruster, The real structure of tobermorite 11A: normal and anomalous forms, OD character and polytypic modifications, Eur. J. Mineral. 13 (2001) 577–590, https://doi.org/10.1127/0935-1221/2001/0013-0577.
[14] K. Momma, F. Izumi, VESTA 3 for three-dimensional visualization of crystal, volumetric and morphology data, J. Appl. Crystallogr. 44 (2011) 1272–1276, https://doi.org/10.1107/S0021889811038970.
[15] C. Biagioni, S. Merlino, E. Bonaccorsi, The tobermorite supergroup: a new nomenclature, Mineral. Mag. 79 (2015) 485–495, https://doi.org/10.1180/minmag.2015.079.2.22.

[16] S. Merlino, E. Bonaccorsi, T. Armbruster, Tobermorites: their real structure and order-disorder (OD) character, Am. Mineral. 84 (1999) 1613–1621, https://doi.org/10.2138/am-1999-1015.

[17] T. Mitsuda, H.F.W. Taylor, Normal and anomalous tobermorites, Mineral. Mag. 42 (1978) 229–235.

[18] W. Loewenstein, The distribution of aluminum in the tetrahedra of silicates and aluminates, Am. Mineral. 39 (1954) 29–96.

[19] S.V. Churakov, C. Labbez, Thermodynamics and molecular mechanism of Al incorporation in calcium silicate hydrates, J. Phys. Chem. C 121 (2017) 4412–4419, https://doi.org/10.1021/acs.jpcc.6b12850.

[20] S. Shaw, S.M. Clark, C.M.B. Henderson, Hydrothermal formation of the calcium silicate hydrates, tobermorite (Ca5Si6O16(OH)2 · 4H2O) and xonotlite (Ca6Si6O17(OH)2): an in situ synchrotron study, Chem. Geol. 167 (2000) 129–140, https://doi.org/10.1016/S0009-2541(99)00205-3.

[21] S.A.S. E⁄-Hemaly, T. Mitsuda, H.F.W. Taylor, Synthesis of normal and anomalous tobermorites, Cem. Concr. Res. 7 (1977) 429–438, https://doi.org/10.1016/0008-8846(77)90071-0.

[22] K. Matsui, J. Kikuma, M. Tsunashima, T. Ishikawa, S.Y. Matsuno, A. Ogawa, M. Sato, In situ time-resolved X-ray diffraction of tobermorite formation in autoclaved aerated concrete: influence of silica source reactivity and Al addition, Cem. Concr. Res. 41 (2011) 510–519, https://doi.org/10.1016/j.cemconres.2011.01.022.

[23] O.P. Shrivastava, F.P. Glasser, Ion-exchange properties of 11-a tobermorite, React. Solids 2 (1986) 261–268.

[24] J. Schreiner, F. Goetz-Neunhoeffer, J. Neubauer, D. Jansen, Hydrothermal synthesis of 11 Å tobermorite – effect of adding metakaolin to the basic compound, Appl. Clay Sci. 185 (2020), 105432, https://doi.org/10.1016/j.clay.2019.105432.

[25] D. Ectors, F. Goetz-Neunhoeffer, J. Neubauer, A generalized geometric approach to anisotropic peak broadening due to domain morphology, J. Appl. Crystallogr. 48 (2015) 189–194, https://doi.org/10.1107/S1600576714026557.

[26] M.D. Jackson, S.R. Chae, S.R. Mulcahy, C. Meral, R. Taylor, P. Li, A.H. Emwas, J. Moon, S. Yoon, G. Vola, H.R. Wenk, P.J.M. Monteiro, Unlocking the secrets of Al-tobermorite in Roman seawater concrete, Am. Mineral. 98 (2013) 1669–1687, https://doi.org/10.2138/am.2013.4484.

[27] W. Liao, W. Li, Z. Fang, C. Lu, Z. Xu, Effect of different aluminum substitution rates on the structure of tobermorite, Materials (Basel) 12 (2019) 1–10, https://doi.org/10.3390/ma12223765.

[28] O.P. Shrivastava, R. Shrivastava, Cation exchange applications of synthetic tobermorite for the immobilization and solidification of cesium and strontium in cement matrix, Bull. Mater. Sci. 23 (2000) 515–520, https://doi.org/10.1007/BF02903893.

[29] N. Hara, N. Inoue, Thermal behaviour of 11Å tobermorite and its lattice parameters, Cem. Concr. Res. 10 (1980) 53–60, https://doi.org/10.1016/0008-8846(80)90051-4.

[30] J. Kikuma, M. Tsunashima, T. Ishikawa, S.Y. Matsuno, A. Ogawa, K. Matsui, M. Sato, In situ time-resolved X-ray diffraction of tobermorite formation process under autoclave condition, J. Am. Ceram. Soc. 93 (2010) 2667–2674, https://doi.org/10.1111/j.1551-2916.2010.03815.x.

[31] M.W. Barnes, B.E. Scheetz, The chemistry of Al-tobermorite and its coexisting phases at 175°C, MRS Proc. 179 (1989) 243–272, https://doi.org/10.1557/PROC-179-243.

[32] V.I. Babushkin, G.M. Matveev, O.P. McHedlov-Petrosian, Thermodynamics of Silicates, Springer-Verlag, 1985.

[33] C.L. Dickson, D.R.M. Brew, F.P. Glasser, Solubilities of CaO – SiO 2 – H 2 O phases at 25 °, 55° and 85° C, Adv. Cem. Res. 16 (2004) 35–43.

[34] S.Y. Hong, Calcium Silicate Hydrate: Crystallisation and Alkali Sorption, University of Aberdeen, 2000.

[35] E. L'Hôpital, B. Lothenbach, D.A. Kulik, K. Scrivener, Influence of calcium to silica ratio on aluminium uptake in calcium silicate hydrate, Cem. Concr. Res. 85 (2016) 111–121, https://doi.org/10.1016/j.cemconres.2016.01.014.

[36] E. L'Hôpital, B. Lothenbach, K. Scrivener, D.A. Kulik, Alkali uptake in calcium alumina silicate hydrate (C-A-S-H), Cem. Concr. Res. 85 (2016) 122–136, https://doi.org/10.1016/j.cemconres.2016.03.009.

[37] S. Barzgar, M. Tarik, C. Ludwig, B. Lothenbach, The effect of equilibration time on Al uptake in C-S-H, Cem. Concr. Res. 144 (2021), 106438, https://doi.org/10.1016/j.cemconres.2021.106438.

[38] F.P. Glasser, J. Pedersen, K. Goldthorpe, M. Atkins, Solubility reactions of cement components with NaCl solutions: I. Ca(OH)2 and C-S-H, Adv. Cem. Res. 17 (2005) 57–64, https://doi.org/10.1680/adcr.2005.17.2.57.

[39] I. Grenthe, J. Fuger, R.J.M. Konings, R.J. Lemire, A.B. Muller, C. Nguyen-Trung, H. Wanner, Chemical Thermodynamics of Uranium, OECD Publications, Paris, France, 2004.

[40] J.D. Cox, D.D. Wagman, V.A. Medvedev, CODATA Key Values for Thermodynamics, Hemisphere Publishing, 1989.

[41] H. Helgeson, J.M. Delany, H.W. Nesbitt, D.K. Bird, Summary and critique of the thermodynamic properties of rock-forming minerals, Am. J. Sci. 278-A (1978).

[42] H.M. Rietveld, A profile refinement method for nuclear and magnetic structures, J. Appl. Crystallogr. 2 (1969) 65–71, https://doi.org/10.1107/S0021889869006558.

[43] D. Jansen, C. Naber, D. Ectors, Z. Lu, X.M. Kong, F. Goetz-Neunhoeffer, J. Neubauer, The early hydration of OPC investigated by in-situ XRD, heat flow calorimetry, pore water analysis and 1H NMR: learning about adsorbed ions from a complete mass balance approach, Cem. Concr. Res. 109 (2018) 230–242, https://doi.org/10.1016/j.cemconres.2018.04.017.

[44] J. Schreiner, F. Goetz-Neunhoeffer, J. Neubauer, S. Volkmann, S. Bergold, R. Webler, D. Jansen, Advanced rietveld refinement and SEM analysis of tobermorite in chemically diverse autoclaved aerated concrete, Powder Diffract. 34 (2019) 143–150, https://doi.org/10.1017/S0885715619000149.

[45] R.W. Cheary, A. Coelho, Fundamental parameters approach to x-ray line-profile fitting, J. Appl. Crystallogr. 25 (1992) 109–121, https://doi.org/10.1107/S0021889891010804.

[46] S.A. Hamid, The crystal structure of the 11A natural tobermorite Ca2.25[Si307.5(OH)1.5] 1H20, Z. Krist. 154 (1981) 189–198.

[47] Y. Le Page, G. Donnay, Refinement of the crystal structure of low-quartz, Acta Cryst 32 (1976) 2456–2459.

[48] E.N. Maslen, V.A. Streltsov, N.R. Streltsova, N. Ishizawa, Electron density and optical anisotropy in rhombohedral carbonates. III. Synchrotron X-ray studies of CaCO3, MgCO3 and MnCO3, Acta Crystallogr. Sect. B 51 (1995) 929–939, https://doi.org/10.1107/S0108768195006434.

[49] J. Schreiner, D. Jansen, D. Ectors, F. Goetz-Neunhoeffer, J. Neubauer, S. Volkmann, New analytical possibilities for monitoring the phase development during the production of autoclaved aerated concrete, Cem. Concr. Res. 107 (2018) 247–252, https://doi.org/10.1016/j.cemconres.2018.02.028.

[50] F. Menges, "Spectragryph - optical spectroscopy software", Version 1.2.15. http://www.effemm2.de/spectragryph/, 2020.

[51] D.A. Kulik, T. Wagner, S.V. Dmytrieva, G. Kosakowski, F.F. Hingerl, K. V. Chudnenko, U.R. Berner, GEM-selektor geochemical modeling package: revised algorithm and GEMS3K numerical kernel for coupled simulation codes, Comput. Geosci. 17 (2013) 1–24, https://doi.org/10.1007/s10596-012-9310-6.

[52] T. Wagner, D.A. Kulik, F.F. Hingerl, S.V. Dmytrievava, GEM-selektor geochemical modeling package: TSolMod library and data interface for multicomponent phase models, Can. Mineral. 50 (2012) 1173–1195, https://doi.org/10.3749/canmin.50.5.1173.

[53] T. Thoenen, W. Hummel, U. Berner, E. Curti, The PSI/Nagra Chemical Thermodynamic Database 12/07 Nuclear Energy and Safety Research Department Laboratory for Waste Management (LES), 2014.

[54] T. Thoenen, D.A. Kulik, Nagra/PSI Chemical Thermodynamic Data Base 01/01 for the GEM-Selektor (V.2- PSI) Geochemical Modeling Code: Release 28-02-03, PSI Internal Report TM-44-03-04, Villingen, Switzerland, 2003.

[55] B.J. Merkel, B. Planer-Friedrich, Groundwater Geochemistry A Practical Guide to Modeling of Natural and Contaminated Aquatic Systems, Springer-Verlag, Berlin, 2008.

[56] D.A. Kulik, Minimising uncertainty induced by temperature extrapolations of thermodynamic data: a pragmatic view on the integration of thermodynamic databases into geochemical computer codes, in: Work. Proc. "The Use Thermodyn. Databases Perform. Assessment" , 29-30th May 2001, Nuclear Energy Agency of the OECD (NEA), Paris, France, Barcelona, Spain, 2002, pp. 125–137. http://inis.iaea.org/search/search.aspx?orig_q=RN:33054563.

[57] G.M. Anderson, D.A. Crerar, Thermodynamics in Geochemistry. The Equilibrium Model, Oxford University Press, New York, USA, 1993.

[58] G. Matekonis, R. Šiaučiunas, D. Vaičiukyniene, Hydrothermal synthesis and characterization of Na+ and [Al3+ + Na+]-substituted tobermorite in CaO-SiO2·nH2O-H2O system, Medziagotyra 16 (2010) 242–248.

[59] X. Qu, Z. Zhao, X. Zhao, Microstructure and characterization of aluminum-incorporated calcium silicate hydrates (C-S-H) under hydrothermal conditions, RSC Adv. 8 (2018) 28198–28208, https://doi.org/10.1039/c8ra04423f.

[60] R.D. Shannon, Revised effective ionic radii and systematic studies of interatomic distances in halides and chalcogenides, Acta Crystallogr. Sect. A. 32 (1976) 751–767, https://doi.org/10.1107/S0567739476001551.

[61] S. Diamond, J.L. White, W.L. Dolch, Effects of isomorphous substitution in hydrothermally-synthesized tobermorite, Am. Mineral. 51 (1966) 388–400.

[62] S. Komarneni, D.M. Roy, C.A. Fyfe, G.J. Kennedy, Naturally occurring 1.4 nm tobermorite and synthetic jennite: characterization by 27Al and 29Si MASNMR spectroscopy and cation exchange properties, Cem. Concr. Res. 17 (1987) 891–895, https://doi.org/10.1016/0008-8846(87)90077-9.

[63] G. Yim, C.S. Yim, Influence of alumina on hydrothermal synthesis of 11A tobermorite, korean, J. Mater. Res. 15 (2005) 97–105.

[64] X. Guo, F. Meng, H. Shi, Microstructure and characterization of hydrothermal synthesis of Al-substituted tobermorite, Constr. Build. Mater. 133 (2017) 253–260, https://doi.org/10.1016/j.conbuildmat.2016.12.059.

[65] P. Yu, R.J. Kirkpatrick, Thermal dehydration of tobermorite and jennite, Concr. Sci. Eng. 97 (2012) 117–119.

[66] J. Skibsted, M.D. Andersen, The effect of alkali ions on the incorporation of aluminum in the calcium silicate hydrate (C-S-H) phase resulting from Portland cement hydration studied by 29Si MAS NMR, J. Am. Ceram. Soc. 96 (2013) 651–656, https://doi.org/10.1111/jace.12024.

[67] I.G. Richardson, A.R. Brough, R. Brydson, G.W. Groves, C.M. Dobson, Location of aluminium in substituted calcium cilicate hydrate (C-S-H) gels as determined by 29Si and 27Al NMR and EELS, J. Am. Ceram. Soc. 76 (1993) 2285–2288.

[68] S.Y. Yang, Y. Yan, B. Lothenbach, J. Skibsted, Incorporation of sodium and aluminum in cementitious calcium-alumino-silicate-hydrate C-(A)-S-H phases studied by 23Na, 27Al and 29Si MAS NMR spectroscopy, J. Phys. Chem. C 125 (2021) 27975–27995.

[69] Z. Wang, S. Ma, S. Zheng, X. Wang, Incorporation of Al and na in hydrothermally synthesized tobermorite, J. Am. Ceram. Soc. 100 (2017) 792–799, https://doi.org/10.1111/jace.14599.

[70] J.A. Tossell, A theoretical study of the molecular basis of the Al avoidance rule and of the spectral characteristics of Al-O-Al linkages, Am. Mineral. 78 (1993) 911–920.

[71] A. Kunhi Mohamed, P. Moutzouri, P. Berruyer, B.J. Walder, J. Siramanont, J. Siramanont, M. Harris, M. Negroni, S.C. Galmarini, S.C. Parker, S.C. Parker, K. L. Scrivener, L. Emsley, P. Bowen, The atomic-level structure of cementitious calcium aluminate silicate hydrate, J. Am. Chem. Soc. 142 (2020) 11060–11071, https://doi.org/10.1021/jacs.0c02988.
[72] I.G. Richardson, G.W. Groves, The incorporation of minor and trace elements into calcium silicate, Cem. Concr. Res. 23 (1993) 131–138.
[73] J. Li, W. Zhang, K. Garbev, G. Beuchle, P.J.M. Monteiro, Influences of cross-linking and Al incorporation on the intrinsic mechanical properties of tobermorite, Cem. Concr. Res. 136 (2020), 106170, https://doi.org/10.1016/j.cemconres.2020.106170.
[74] Y. Yan, S.-Y. Yang, G.D. Miron, I. Collings, . LHopital, J. Skibsted, F. Winnefeld, K. Scrivener, B. Lothenbach, Effect of alkali hydroxide on calcium silicate hydrate (C-S-H), Cem. Concr. Res. 151 (2022), 106636, https://doi.org/10.1016/j.cemconres.2021.106636.
[75] R.J. Myers, E. L'Hôpital, J.L. Provis, B. Lothenbach, Composition-solubility-structure relationships in calcium (alkali) aluminosilicate hydrate (C-(N, K-)A-S-H), Dalton Trans. 44 (2015) 13530–13544, https://doi.org/10.1039/c5dt01124h.
[76] R. Gabrovšek, B. Kurbus, D. Mueller, W. Wieker, Tobermorite formation in the system CaO, C3S-SiO2-Al2O3-NaOH-H2O under hydrothermal conditions, Cem. Concr. Res. 23 (1993) 321–328, https://doi.org/10.1016/0008-8846(93)90097-S.
[77] A. Majdinasab, Q. Yuan, Synthesis of Al-substituted 11Å tobermorite using waste glass cullet: a study on the microstructure, Mater. Chem. Phys. 250 (2020), https://doi.org/10.1016/j.matchemphys.2020.123069.
[78] G.K. Sun, J.F. Young, R.J. Kirkpatrick, The role of Al in C-S-H: NMR, XRD, and compositional results for precipitated samples, Cem. Concr. Res. 36 (2006) 18–29, https://doi.org/10.1016/j.cemconres.2005.03.002.
[79] E. Lippmaa, A. Samoson, M. Mägi, High-resolution 27A1 NMR of aluminosilicates, J. Am. Chem. Soc. 108 (1986) 1730–1735, https://doi.org/10.1021/ja00268a002.
[80] D. Sykes, J.D. Kubicki, T.C. Farrar, Molecular orbital calculation of 27Al and 29Si NMR parameters in Q3 and Q4 aluminosilicate molecules and implications for the interpretation of hydrous aluminosilicate glass NMR spectra, J. Phys. Chem. A 101 (1997) 2715–2722, https://doi.org/10.1021/jp963891z.
[81] C.I. Merzbacher, B.L. Sherriff, J.S. Hartman, W.B. White, A high-resolution 29Si and 27Al NMR study of alkaline earth aluminosilicate glasses, J. Non-Cryst. Solids 124 (1990) 194–206, https://doi.org/10.1016/0022-3093(90)90263-L.
[82] D.R. Neuville, L. Cormier, V. Montouillout, D. Massiot, Local Al site distribution in aluminosilicate glasses by 27Al MQMAS NMR, J. Non-Cryst. Solids 353 (2007) 180–184, https://doi.org/10.1016/j.jnoncrysol.2006.09.035.
[83] S. Kucharczyk, M. Zajac, C. Stabler, R.M. Thomsen, M. Ben Haha, J. Skibsted, J. Deja, Structure and reactivity of synthetic CaO-Al 2 O 3 -SiO 2 glasses, Cem. Concr. Res. 120 (2019) 77–91, https://doi.org/10.1016/j.cemconres.2019.03.004.
[84] R.M. Thomsen, J. Skibsted, Y. Yue, The charge-balancing role of calcium and alkali ions in per-alkaline aluminosilicate glasses, J. Phys. Chem. B 122 (2018) 3184–3195, https://doi.org/10.1021/acs.jpcb.7b12437.
[85] G. Renaudin, J. Russias, F. Leroux, C. Cau-dit-Coumes, F. Frizon, Structural characterization of C-S-H and C-A-S-H samples-part II: local environment investigated by spectroscopic analyses, J. Solid State Chem. 182 (2009) 3320–3329, https://doi.org/10.1016/j.jssc.2009.09.024.
[86] G. Renaudin, J. Russias, F. Leroux, F. Frizon, C. Cau-dit-Coumes, Structural characterization of C-S-H and C-A-S-H samples-part I: long-range order investigated by rietveld analyses, J. Solid State Chem. 182 (2009) 3312–3319, https://doi.org/10.1016/j.jssc.2009.09.026.
[87] N.V. Chukanov, Infrared Spectra of Mineral Species: Extended Library, Springer, Dordrecht, 2014, https://doi.org/10.1007/978-94-007-7128-4.
[88] A. Vidmer, G. Sclauzero, A. Pasquarello, Infrared spectra of jennite and tobermorite from first-principles, Cem. Concr. Res. 60 (2014) 11–23, https://doi.org/10.1016/j.cemconres.2014.03.004.
[89] P. Yu, R.J. Kirkpatrick, B. Poe, P.F. McMillan, X. Cong, Structure of calcium silicate hydrate (C-S-H): near-, mid-, and far-infrared, Spectroscopy 48 (1999) 742–748.
[90] I.G. Richardson, J. Skibsted, L. Black, R.J. Kirkpatrick, Characterisation of cement hydrate phases by TEM, NMR and raman spectroscopy, Adv. Cem. Res. 22 (2010) 233–248, https://doi.org/10.1680/adcr.2010.22.4.233.
[91] R.J. Kirkpatrick, J.L. Yarger, P.F. McMillan, P. Yu, X. Cong, Raman spectroscopy of C-S-H, tobermorite, and jennite, Adv. Cem. Based Mater. 5 (1997) 93–99, https://doi.org/10.1016/S1065-7355(97)00001-1.
[92] K. Garbev, P. Stemmermann, L. Black, C. Breen, J. Yarwood, B. Gasharova, Structural features of C-S-H(I) and its carbonation in air-a raman spectroscopic study. Part I: fresh phases, J. Am. Ceram. Soc. 90 (2007) 900–907, https://doi.org/10.1111/j.1551-2916.2006.01428.x.
[93] S. Ortaboy, J. Li, G. Geng, R.J. Myers, P.J.M. Monteiro, R. Maboudian, C. Carraro, Effects of CO2 and temperature on the structure and chemistry of C-(A-)S-H investigated by raman spectroscopy, RSC Adv. 7 (2017) 48925–48933, https://doi.org/10.1039/c7ra07266j.
[94] H.W. Nesbitt, C. O`Shaughnessy, G.S. Henderson, G.M. Bancroft, D.R. Neuville, Factors affecting line shapes and intensities of Q3 and Q4 Raman bands of Cs silicate glasses, Chem. Geol. 505 (2019) 1–11, https://doi.org/10.1016/S1065-7355(97)00001-1.
[95] J.H. Park, Effect of silicate structure on thermodynamic properties of calcium silicate melts: quantitative analysis of raman spectra, Met. Mater. Int. 19 (2013) 577–584, https://doi.org/10.1007/s12540-013-3028-4.
[96] V. Ranieri, D. Bourgogne, S. Darracq, M. Cambon, J. Haines, O. Cambon, R. Leparc, C. Levelut, A. Largeteau, G. Demazeau, Raman scattering study of α -quartz and Si1-x gex O2 solid solutions, Phys. Rev. B - Condens. Matter Mater. Phys. 79 (2009) 1–9, https://doi.org/10.1103/PhysRevB.79.224304.
[97] P.F. McMillan, G. Wolf, P. Lambert, A raman spectroscopic study of shocked single crystalline quartz, Phys. Chem. Miner. 19 (1992) 71–79.
[98] N.Y. Mostafa, A.A. Shaltout, H. Omar, S.A. Abo-El-Enein, Hydrothermal synthesis and characterization of aluminium and sulfate substituted 1.1 nm tobermorites, J. Alloys Compd. 467 (2009) 332–337, https://doi.org/10.1016/j.jallcom.2007.11.130.
[99] S. Barzgar, B. Lothenbach, M. Tarik, A. Di Giacomo, C. Ludwig, The effect of sodium hydroxide on Al uptake by calcium silicate hydrates (C-S-H), J. Colloid Interface Sci. 572 (2020) 246–256, https://doi.org/10.1016/j.jcis.2020.03.057.
[100] L. Pegado, C. Labbez, S.V. Churakov, Mechanism of aluminium incorporation into C-S-H from ab initio calculations, J. Mater. Chem. A 2 (2014) 3477–3483, https://doi.org/10.1039/c3ta14597b.
[101] C.L. Dickson, D.R.M. Brew, F.P. Glasser, Solubilities of Crystalline Calcium Silicate Hydrates, Final Report NIREX, UK, Didcot, UK, 2002.